# Nanotubes from the misfit layered compound $(SmS)_{1.19}TaS_2$: Atomic structure, charge-transfer and electrical properties

M. B. Sreedhara,[1] Kristýna Bukvišová,[2] Azat Khadiev,[3] Daniel Citterberg,[2] Hagai Cohen,[4] Viktor Balema,[5,6] Arjun K. Pathak,[7] Dmitri Novikov,[3] Gregory Leitus,[4] Ifat Kaplan-Ashiri,[4] Miroslav Kolíbal,[2,8*] Andrey N. Enyashin,[9,10] Lothar Houben,[4*]and Reshef Tenne[1*]

*(Dedicated to Professor John B. Goodenough on the Occasion of his 100th year Birthday. Until hundred and twenty like twenty -a proverb in Hebrew)*

[1]Department of Molecular Chemistry and Materials Science, Weizmann Institute of Science, Rehovot 7610001, Israel
[2]CEITEC – Central European Institute of Technology, Brno University of Technology, Purkyňova 123, 612 00 Brno, Czech Republic
[3]Deutsches Elektronen-Synchrotron DESY, Notkestr. 85, 22607 Hamburg, Germany
[4]Department of Chemical Research Support, Weizmann Institute, Rehovot 7610001, Israel
[5]Ames Laboratory, U.S. Department of Energy, Ames, IA, 50011-3020, USA
[6]ProChem, Inc. 826 Roosevelt Road Rockford, IL 61109, USA
[7]Department of Physics, SUNY Buffalo State, Buffalo, New York 14222, USA
[8]Institute of Physical Engineering, Brno University of Technology, Technická 2, 616 69 Brno, Czech Republic
[9]Institute of Solid State Chemistry UB RAS, 620990 Ekaterinburg, Russian Federation
[10]Ural Federal University, Institute of Natural Sciences and Mathematics, 620083 Ekaterinburg, Russian Federation

[*]corresponding authors- reshef.tenne@weizmann.ac.il, lothar.houben@weizmann.ac.il, kolibal.m@fme.vutbr.cz

**Abstract**

Misfit layered compounds MX-$TX_2$, where M, T= metal atoms; X = S, Se or Te, (MLC) and their nanotubes are of significant interest due to their rich chemistry and unique quasi-1D structure. In particular, Ln-$TX_2$ (Ln= rare-earth atom) constitute a relatively large family of MLC, from which nanotubes have been synthesized. The properties of MLCs can be tuned by the chemical and structural interplay between LnX and $TX_2$ sub-layers and alloying of each of the Ln, T and X elements. In order to engineer them to gain desirable performance, a detailed understanding of their complex structure is indispensable. MLC nanotubes are a relatively new-comer and offer new opportunities. In particular, like $WS_2$ nanotubes before, the confinement of the free-carriers in these quasi-1D nanostructures and their chiral nature offer intriguing physical behavior. High-resolution transmission electron microscopy in conjunction with a focused ion beam are engaged to study SmS-$TaS_2$ nanotubes and their cross-sections at the atomic scale. The atomic resolution images distinctly reveal that Ta is in trigonal prismatic coordination with S atoms in a hexagonal structure. Furthermore, the position of the sulfur atoms in both the SmS and the $TaS_2$ sub-lattices, is revealed. X-ray photoelectron spectroscopy, electron-energy loss spectroscopy and X-ray absorption spectroscopy are carried out. These analyses conclude that charge transfer from the Sm to the Ta atoms leads to filling of the Ta $5d_{z^2}$ level, which is confirmed by density functional theory (DFT) calculations. Transport measurements show that the nanotubes are semimetallic with resistivities in the range of $10^{-4}$ Ω□cm at room temperature and magnetic susceptibility measurements show a superconducting transition at 4 K.

## Introduction

Misfit layered compounds (MLCs) are a class of two-dimensional (2D) materials receiving considerable attention due to their unique structure; crystallographic diversity and chemically tailorable characteristics (*vide infra*).[1-8] Among the MLCs, the chalcogenides-based MLCs are of special interest due to their metallic and semiconducting properties. The chalcogenides-based MLCs with the general formula $(MX)_{1+y})_m(TX_2)_n$ with M=Sn, Sb, Pb, Bi; Ln-rare earth, Y; T= Ta, Nb, V, Cr and X is a chalcogen atom S, Se, Te constitute a superstructure of alternating slabs of distorted rocksalt MX and hexagonal $TX_2$ structural units (see **Fig. 1**a-d). For the most common case, it is abbreviated as MX-$TX_2$ (m=n=1). Another shortened notation for MLC often used in the literature is (*O-T),* indicating orthorhombic (*O*= MX) and trigonal prismatic (*T*= $TX_2$) coordination respectively.

With their unique structure and tunable properties, chalcogenides-based MLCs offer potential applications in thermoelectrics.[9-13] In order to tune the desired character of MLC such as electronic conductivity or phonon scattering and improve their thermoelectric performance, a detailed structural understanding of each sublayer (MX and $TX_2$) atom by atom is highly desirable. Further, the periodic modulation due to non-stoichiometry and misfit strain can create strain waves and lead to vacancies in the structure (especially in the rocksalt unit), which may induce Anderson localization in these compounds.[14] Advancement in sub-angstrom resolution electron microscopy and growth techniques [15, 16] in recent times have prompted research into their local structure, charge transfer characteristics, and spectroscopic properties. The inception of misfit nanotubes over the last decade brought about another twist to their study.[17-19]

Due to their 1D structure and chiral nature, nanotubes of inorganic layered compounds, like $WS_2$ offer intriguing physical properties,[20, 21] making the study of MLC nanotubes also highly warranted. MLC nanotubes of the kind SnS-$SnS_2$ were first obtained serendipitously by laser ablation of $SnS_2$ powder.[22] Later-on rare-earth-based LnS-$TaS_2$ (Ln= rare-earth atom) MLCs and their nanotubes have been studied quite extensively.[17, 23-27] LnS-$TaS_2$ MLC constitute a large family of compounds and are rather interesting owing to the significant charge transfer from the LnS unit to $TaS_2$. The unique optical and magnetic properties of rare-earth compounds offer numerous potential applications, making the study of lanthanide-based MLC nanotubes highly warranted.

Among the LnS-$TaS_2$ family, SmS-$TaS_2$ is of special interest due to the exotic physical properties of their binary sulfide constituents (*vide infra*).[7, 8, 28, 29] The binary SmS shows switching behavior, i.e. an ability to undergo reversible pressure-induced (at 6.5 kbar) semiconductor-to-metal transition at room temperature, which can be switched back to its original phase upon heating.[28, 30-32] As a result Sm can accommodate two ground states configurations, either nonmagnetic $Sm^{2+}$ (semiconducting SmS) with $4f^6$ ($^7F_0$) configuration or in the magnetic $Sm^{3+}$ (metallic SmS) with $4f^5$ ($^6H_{5/2}$) configuration.[33] Interestingly, in addition to the properties of SmS, the abundant electron coupling interactions in the 2H-$TaS_2$ lead to compelling physical phenomena such as layer-dependent charge density waves [29] and interfacial superconductivity.[34] The combination of these physical properties from the respective binary phases and the atomic-scale manipulation of charge transfer in $(SmS)_{1.19}TaS_2$ can tune the electronic quantum phases, which could result in new physical observations. The binary SmS crystallizes in a rocksalt structure with the space group *Fm-3m* (*a*= 5.97 Å, for $Sm^{2+}$, and *a*= 5.57 Å, for the high-pressure phase, $Sm^{3+}$), where Sm atoms are octahedrally coordinated to S atoms. 2H-$TaS_2$ is a layered compound with hexagonal lattice (*a* = 3.314 Å, *c* = 12.097 Å, $P6_3/mmc$) in which each Ta atom is bound to six sulfur atoms in a trigonal

prismatic configuration.[35] The structural motifs of SmS-$TaS_2$ can be described in the orthorhombic space group *Fm2m* with *FF* centering,[7] in which SmS and $TaS_2$ are stacked layer by layer periodically along *c*-axis (*a*=3.29 Å, *b*=5.67 Å and *c*=22.50 Å). Given the unit-cell dimensions of each sub-lattice, the misfit ratio- *y* of the compound $(SmS)_{1+y}TaS_2$ can be found from the formula $1+y=2a_{TaS2}/a_{SmS}$ to be 1.19. This factor represents also the deviation from the stoichiometry of the two sub-units in the MLC. Previously, the SmS-$TaS_2$ MLC was investigated using scanning tunneling micro(spectro)scopy and it was concluded that the outermost layer on the surface of the cleaved crystal is SmS.[36] On the other hand, high-resolution transmission electron microscopy (HRTEM) revealed that the outermost layer of MLC is the $TaS_2$ layer.[37] Also, the $(SmS)_{1.19}TaS_2$ surface was found to be semimetallic.[36, 38]

The charge transfer, from LnS to $TaS_2$ stabilizes MLC structures and alters the electronic properties of the two sub-units, appreciably.[39] The amount of charge transfer can be tuned by alloying the rocksalt (LnS) unit with other rare earth or hetero-atoms. [40, 41] The role of the charge transfer from the Ln atoms to the Ta atoms has been elucidated.[25, 41] In particular, since the work function of the LnS sub-unit is smaller than that of the hexagonal $TaS_2$, charge transfer occurs from the rare-earth atom to the partially occupied $5d_Z^2$ level of the tantalum atom. This charge transfer modifies the effective valence state of the rare-earth atom (2+) closer to the more stable 3+ state. Furthermore, the $5d_Z^2$ level of the Ta atom, which dominates the density of states (DOS) at the Fermi level ($E_f$), is getting almost filled by the charge transfer.[39, 42] This effect leads to an increase in the density of occupied states at the $E_f$ and reduces the hole conductivity. The charge transfer also stabilizes 2H (trigonal prismatic coordination) polytype of $TaS_2$ preventing its transformation into 1T with octahedral coordination and the ensuing charge density wave transition. This conjecture was supported by Raman spectroscopy of individual nanotubes.[27] Nonetheless, direct evidence from transmission electron microscopy with the sub-angstrom resolution was missing so far and is presented here.

In the present work, nanotubes (and flakes) of the misfit compound $(SmS)_{1.19}TaS_2$ were studied in detail to address the structural aspects atom by atom and correlate it with its properties. High-resolution transmission electron microscopy with the sub-Ångstrom resolution was employed here to elucidate the atomic arrangements in the lattice of $(SmS)_{1.19}TaS_2$ nanotubes, which was not available before. Moreover, by using dual-beam focused ion beam microscopy (FIB), lamellae of such nanotubes were prepared to enable direct imaging of the superstructure from the axial *b* direction (nanotube growth axis). This analysis yields the lattice structure of such MLC nanotubes in unprecedented detail and provides a pathway to correlate the structure with the physical properties of such 1D nanostructures.

X-ray photoelectron spectroscopy (XPS) and high-resolution electron energy loss spectroscopy (HR-EELS) were employed here to elucidate the core levels and valence band structure of the $(SmS)_{1.19}TaS_2$ MLC nanotubes and flakes, and pure 2H-$TaS_2$. It was shown that the $5d_Z^2$ level of Ta in MLC is getting filled-up upon coupling with SmS and the charge transfer from Sm→Ta. The filling of Ta $5dz^2$ and valence conversion of $Sm^{2+}$ to $Sm^{3+}$ upon charge transfer was further confirmed by X-ray absorption (XAS) studies. These observations were validated with DFT calculations. Magnetic susceptibility measurements at low temperature show that $(SmS)_{1.19}TaS_2$ is superconducting below 5K while the four-probe electrical measurements at room temperature show a semimetallic behavior of the nanotubes.

## Results and discussion

As illustrated in **Fig. 1**a and e, the rocksalt SmS structure in the MLC is modulated compared to pristine SmS (**Fig. 1**d) whereas the hexagonal $TaS_2$ is almost undistorted resembling bulk 2H-$TaS_2$. The SmS slab is made of only half a unit cell (along the *c*-axis) between the two $TaS_2$ units of MLC. The Sm is coordinated to only five sulfur atoms (instead of six in the binary SmS) within the unit (**Fig. 1**e) and consequently may have a strong dipolar interaction with sulfur atoms of the adjacent

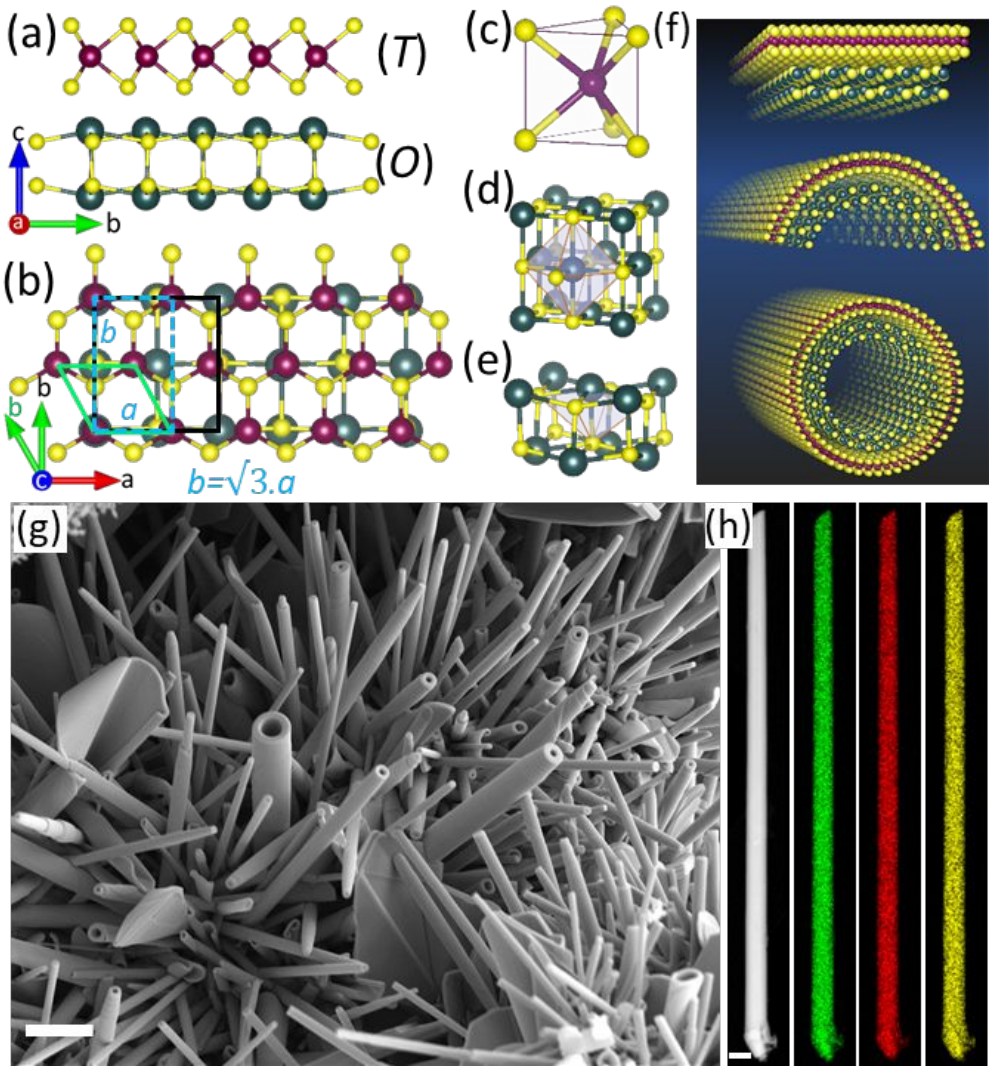


***Fig. 1. Structure, morphology, and chemical analyses of misfit $(SmS)_{1.19}TaS_2$.*** *Schematic drawing of the MLC lattice structure projected in a-b plane (a) and along the c-direction (b), respectively. In a-b plane, the incommensurate-a, and commensurate-b crystallographic axes of the ortho-hexagonal unit cell ($b=\sqrt{3}.a$) were marked in cyan color. The O and T represent orthorhombic and trigonal prismatic coordination of Sm in the rocksalt unit and Ta in the hexagonal unit and are graphically represented in (c) and (d), respectively. Single-layer MLC slab constitutes half a unit cell of rocksalt structure and is graphically shown in (e) with corresponding coordination of Sm. (f) Graphical rendering of the formation mechanism of an MLC nanotube via misfit strain relaxation (folding) and seaming of the rim atoms. (g) SEM image of $(SmS)_{1.19}TaS_2$ flakes and nanotubes obtained by quenching high-temperature CVT reaction to ambient conditions, scale bar is 2 µm. (h) STEM HAADF images of a single $(SmS)_{1.19}TaS_2$ MLC nanotube and corresponding SEM-EDS chemical maps (Sm- green, Ta- red, and S- yellow), scale bar 200 nm.*

$TaS_2$. MLC compounds tend to roll into nanotubes due to the misfit strain (between the rocksalt MX and hexagonal $TX_2$ layers) and seaming of the dangling bonds at the rim atoms.[43] The folding mechanism is schematically depicted in **Fig. 1**f. The MLC nanotubes of $(SmS)_{1.19}TaS_2$ were produced by a well-established chemical vapor transport protocol with slight modification in growth temperature to improve the yield. SEM micrographs of as-obtained $(SmS)_{1.19}TaS_2$ powder displayed in **Fig. 1**h and **S1**a show nanotubular structures as a major product. The other common byproducts such as flakes and nanoscrolls with similar chemical compositions (as confirmed by SEM-EDS) were also observed. Semi-quantitative EDS analysis showed that the stoichiometry of the nanotubes is $(SmS)_{1.05}TaS_2$. The majority of the nanotubes display constant diameter along the tube axis whereas few of them showed telescopic contour with varying diameters along the tube axis. SEM analysis revealed that the MLC tubes are grown perfectly under the established reaction conditions. It will be interesting to know what thermodynamic and kinetic factors could lead to either type of morphology such as nanotube/nanoscroll but none of the *ex-situ* measurements could reveal those conditions. Statistical analysis of the nanotubes size distribution was carried out using SEM images. This analysis revealed that the nanotubes display varying lengths and the majority of them falling within the range of 100 to 200 nm in diameter. **Fig. 1**h shows low magnification scanning transmission electron microscopy (STEM) and STEM-EDS chemical maps of single $(SmS)_{1.19}TaS_2$ nanotube (see also **Fig. S1**b). The nanotube is 200 nm in diameter and the size of the tube is uniform along its entire length. The chemical maps reveal the uniform distribution of samarium (red), tantalum (green), and sulfur (yellow) elements throughout the tube. Quantitative STEM-EDS analysis of several nanotubes and flakes (**Fig. S1**c,d**)** show the stoichiometry $(SmS)_{1.08}TaS_2$ and $(SmS)_{1.05}TaS_2$, respectively, which are quite comparable to the theoretical value $1+y=1.19$. Deviations are attributed to the experimental error as well as structural defects (*vide infra*). No signal, which could be associated with oxidation of the nanotube core was obtained. Slight and somewhat nonuniform surface oxide layer (< 1 nm) was occasionally observed.

X-ray diffraction (XRD) of $(SmS)_{1.19}TaS_2$ powder exhibits a strong diffraction pattern with a highly preferred orientation along the *c*-direction (see **Fig. S2**). The observed patterns are consistent with an earlier report[7] and the interlayer spacing calculated from the (*002*) periodicity is 11.3 Å equivalent to c/2 of *FF* centered $(SmS)_{1.19}TaS_2$ misfit lattice. The strongly preferred orientations along <*00l*> direction are characteristics of freestanding (*O-T*) superstructures which are grown seamlessly along the *c*-direction. In addition to the regular (*00l*) peaks with periodicities of 11.3 Å, the XRD pattern exhibits weaker reflections with periodicities of 17.2 Å, typical for the (*O-T-T*) superstructure.[37] Indeed the purely (*O-T-T*) order in a nanotube/flakes generates a new compound i.e. $(SmS)_{1.19}(TaS_2)_2$. Here, the (*O-T-T*) order was interspersed, sporadically, between the (*O-T*) superstructure and was probably caused by the defects in the SmS unit. The relative intensity of (002) planes of (*O-T*) and (*O-T-T*) structure in XRD yields 4% of (*O-T-T*) layers in the overall compound. It is worth mentioning that a systematic transformation from (*O-T*), i.e. $(LaS)_{1.14}(TaS_xSe_{1-x})_2$ to (*O-T-T*)- $(LaS)_{1.14}(TaSe_2)_2$ MLC occurred upon increasing the selenium to the sulfur ratio in the asymmetric misfit system.[37] Further, the X-ray diffraction data (**Fig. S2**) does not reveal any characteristic peaks for impurities, such as binary sulfides ($SmS/TaS_2$) and elemental Sm/Ta/S in the reaction products within its sensitivity limit.

Transmission electron microscopy (TEM) analysis reported in previous studies[27] did not have sufficient resolution to reveal the finest details of the structure of these nanotubes. Therefore, in the present work, the nanotubes were analyzed via TEM techniques with the highest possible resolution. Several $(SmS)_{1.19}TaS_2$ nanotubes were examined here. The results for one such

nanotube are displayed in **Fig. 2** (see also **Fig. S3** and **S4**). A low magnification image of the nanotube in the inset of **Fig. 2a** shows a constant diameter of 170 nm along its entire length. The

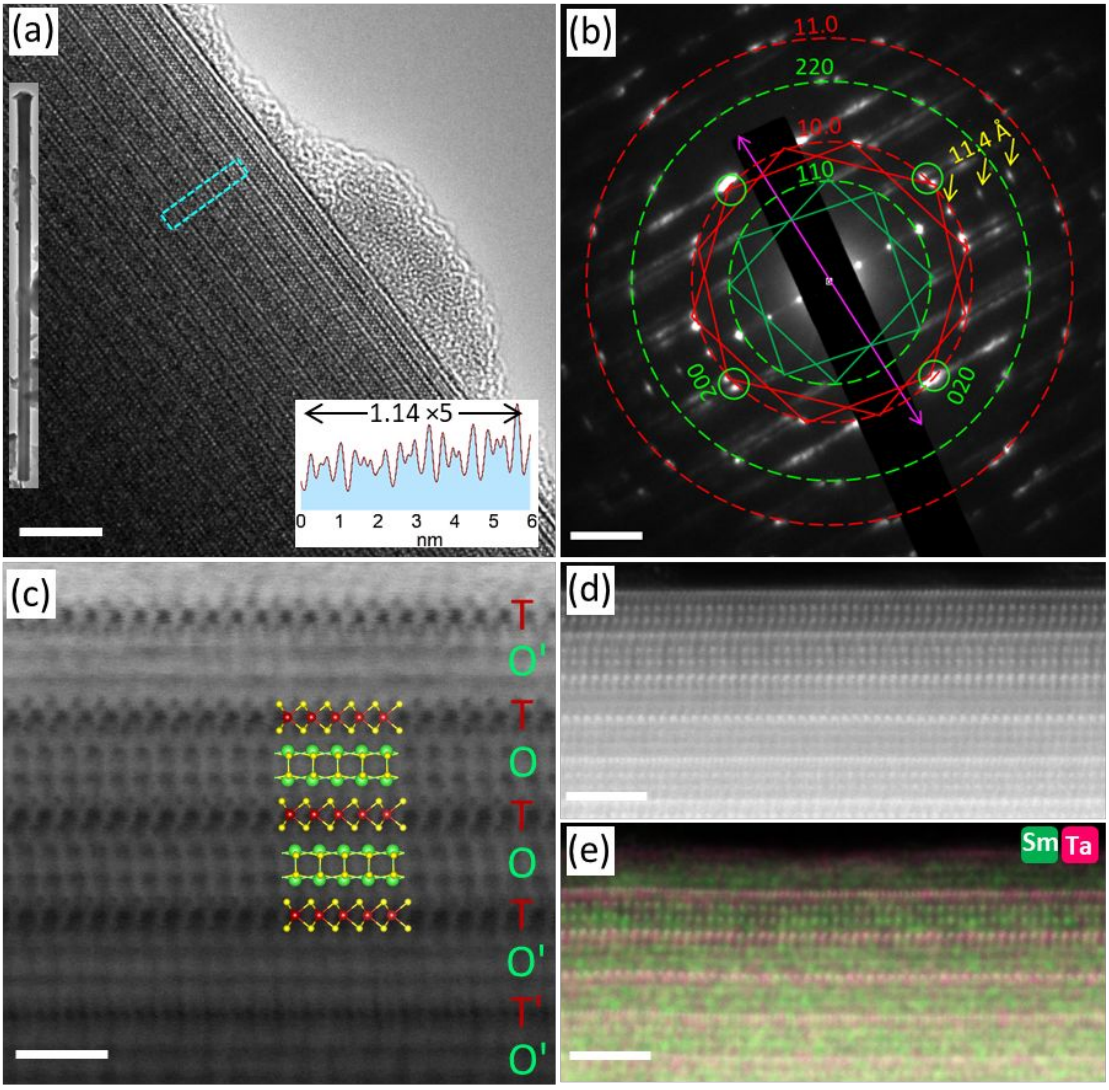


***Fig. 2**. **TEM images, electron diffraction and chemical analyses** of a $(SmS)_{1.19}TaS_2$ nanotube. (a) High-resolution TEM image. The periodic stacking of SmS and $TaS_2$ layers in the misfit structure is revealed with $TaS_2$ as the outermost layer. Scale bar is 5 nm. The low magnification image of the nanotube (diameter 170 nm) and an intensity line profile perpendicular to the tube axis are shown in insets. (b) SAED pattern acquired from part of an individual nanotube. The sets of diffraction spots corresponding to SmS and $TaS_2$ are marked with green and red dotted circles. The respective Miller indices are indicated. Small yellow arrows indicate basal plane reflections and the tubule axis is marked by the purple double-headed arrow. The two sets of four pairs (110) reflections of the rocksalt SmS subsystem are marked by rotated green squares. The two sets of six pairs (10.0) reflections of the orthohexagonal $TaS_2$ sub-lattice are marked by red hexagons. These sets of reflections are rotated by 30° with respect to each other. (c) Atomically resolved HR-STEM image of a few (O-T) layers near the surface of the nanotube. The scale bar is 1 nm. The corresponding atomic model is overlaid on the HR-STEM image. The 30° rotation of (O-T)(O-T)' layers is clearly visible. Yellow, red, and green spheres represent S, Ta, and Sm atoms respectively. (d) STEM-HAADF image and overlaid (e) STEM-EDS elemental maps Sm (red) and Ta (cyan) of a few layers from the surface of the tube, scale bar 2 nm.*

high-resolution TEM image of the SmS-$TaS_2$ superstructure reveals a periodic stacking sequence of SmS and $TaS_2$ along the *c*-direction. The outermost layer is $TaS_2$, which is true for all the

nanotubes analyzed here as well as other Ln-based misfit nanotubes. Note that potential sources of damage prior to investigation, such as plasma cleaning, were avoided to preserve the pristine surface of the nanotubes. Previously, an STM study of the cleaved surface of SmS-$TaS_2$ shows that SmS is the surface layer,[36] but that observation may have resulted from the cleavage process.[36] The surfaces of the nanotubes analyzed here are almost intact and unlike LaS-$TaS_2$, [44] do not show any, or little oxidation. The intensity profile drawn perpendicular to the tube axis (along *c*) shown in the inset reveals that the periodicity of the single-layer MLC unit is 11.4 Å, which is in close agreement with the (*00l*) reflection of the corresponding (*O-T*) structure observed from XRD.

Selected area electron diffraction (SAED) pattern of an individual $(SmS)_{1.19}TaS_2$ nanotube is displayed in **Fig. 2b**. The intense and distinguished spots indicate ordered stacking of the SmS and $TaS_2$ layers in the misfit lattice. The ED pattern reveals a pair of four-fold and a pair of six-fold periodicity for rocksalt SmS and hexagonal $TaS_2$ sublattices respectively, which are rotated by 30° with respect to each other. Two sets of four pairs of spots that are azimuthally equally distributed with the interplanar spacings of 1.85 Å and 3.7 Å (on the green circle) were assigned to the (110) and (220) planes of rocksalt SmS. Two sets of six pairs of spots (on the red circles) with the interplanar spacings 1.6 and 2.85 Å are attributed to hexagonal $TaS_2$. These azimuthally equally distributed sets of quartet and sextet spots (marked by green squares and red hexagons-rotated by 30°) indicate two folding vectors for both SmS and $TaS_2$ layers in the nanotube. This results in the formation of super periodicity of the kind (*O-T*)(*O-T*)' and is reminiscent of the *CF* and *FF* superstructure in MLC (*vide infra*).[45] The angular splitting of the spots into pairs is due to a small chiral angle of the nanotube (≈ 3 deg). The (020) reflections of SmS, which coincide with the (10.0) reflections of $TaS_2$ (marked by a small green circle), reveal the common commensurate *b*-axis. The (020) and (200) reflections of SmS are approximately placed on the same dotted circle and are perpendicular to each other. This observation confirms that the *a* and *b* lattice parameters of SmS are (almost) equal. In the present nanotube, the common commensurate *b* axis appears 15° off from the nanotube growth axis. In many other nanotubes, the commensurate *b* axis coincide with the tube axis (see **Fig**. **S3**). The basal plane reflections indicated by yellow arrows reveal the periodicity of 11.4 Å along the *c*-direction. In general, the nanotubes of $(SmS)_{1.19}TaS_2$ prepared in this study exhibit a high degree of crystallinity, and the superstructure of SmS and $TaS_2$ is well preserved.

The atomic structure of the nanotubes was analyzed with high-resolution scanning transmission electron microscopy (HR-STEM) and STEM- energy-dispersive X-ray spectroscopy (EDS) (**Fig. 2**c-e and **Fig. S4**). The atomically resolved STEM bright-field (BF) image in **Fig. 2**c reveals that the nanotubes are comprised of (*O-T*) and (*O-T*)' layers with high stacking order. The contrast difference between (*O-T*) and (*O-T*)' layers is clearly visible indicating the two different crystallographic orientations of the misfit layers. The interatomic distances in the projection reveal different orientations of the $TaS_2$ in the nanotube, the viewing directions are along <10.0> and <11.0>. Similarly, the orientation of the SmS layer can be linked to <100> and <110> directions which are in line with the ED results. In many nanotubes of this kind, the (*O-T*) pairs seem to be tilted in 30° with respect to the adjacent (*O-T*)' wall forming thereby a super-periodicity of the kind (*O-T*)(*O-T*)' as confirmed by ED. The reason for the tilting of (*O-T*) layers is unknown, though. A possible explanation is that quenching from the high temperature to room temperature in the synthesis may have arrested the reorganization of layers in the nanotube. Alternatively, the misfit lattice may prefer this unique orientation to minimize the misfit strain. The two different orientations in the nanotube tend to alternate along the common *c*-axis leading to double periodicity with 23 Å as the unit distance of the supercell (**Fig 2**c and **2**d**)**. The first two layers being

(*O-T*) i.e. <10.0> $TaS_2$ and <100> SmS and the adjacent layers are oriented 30° designated as (*O-T*)', i.e. <11.0> $TaS_2$ and <110> SmS, respectively. There is stronger contrast of the (*O-T*) layers over the (*O-T*)' layers. The difference in contrast is related to orientation-dependent channeling phenomena and not to composition. Careful analysis of the atomic arrangement reveals that $TaS_2$ lattice consists of a chevron-type pattern where the sulfur atoms are coordinated with the Ta atoms in trigonal prismatic fashion, i.e. 1H polytype. Generally, quenching of $TaS_2$ from such a high temperature would lead to 1T polytype.[46] The stability of 1H-$TaS_2$ in the $(SmS)_{1.19}TaS_2$ MLC can be attributed to strong charge transfer from SmS to $TaS_2$, which is further confirmed by spectroscopic techniques (*vide infra*). The SmS subunit is arranged in a distorted rocksalt structure. In the <100> viewing direction of the SmS the sulfur atoms sit at a small projected distance from the samarium, and consequently in this orientation sulfur and samarium positions are not as well resolved as below (see **Fig. 4**b). The representative atomic models of <10.0> $TaS_2$ and <100> SmS are overlaid on the HR-STEM image for clarity. HR-STEM (DF) image and the corresponding HR-STEM-EDS

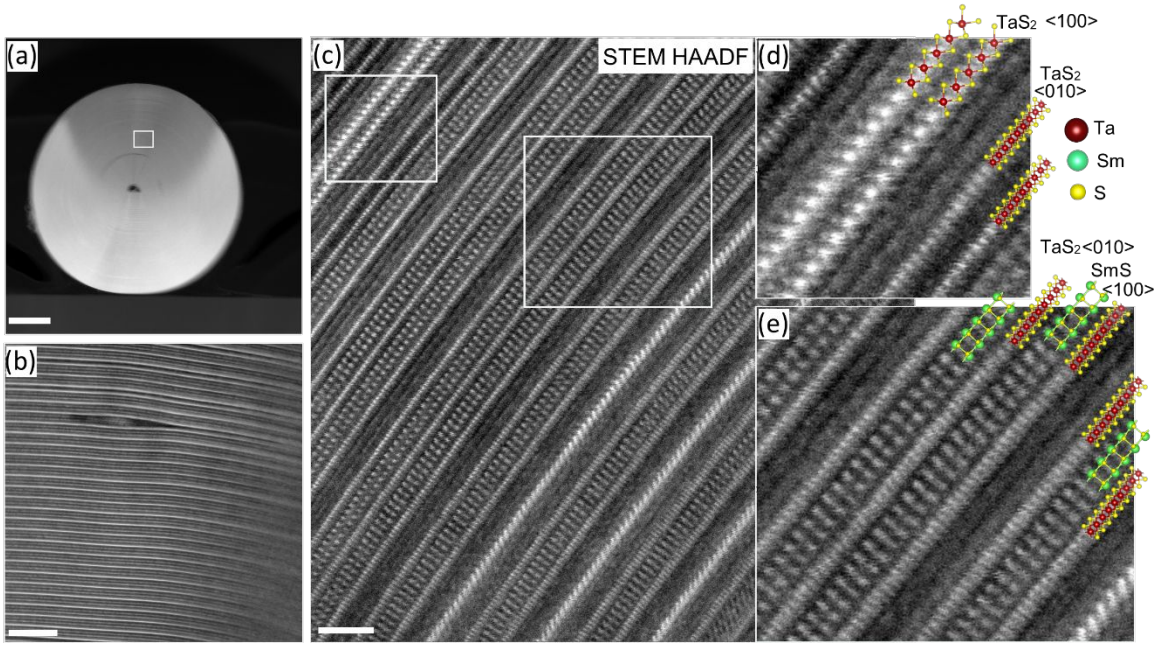


***Fig. 3.*** *STEM analysis of cross-sectioned FIB lamella of $(SmS)_{1.19}TaS_2$ nanotube (a) Low magnification STEM-BF image of nanotube lamella, scale bar is 100 nm. (b) High magnification STEM-HAADF image of a portion of the cross-section showing the basic MLC backbone (O-T) structure, the defect layer of SmS ending abruptly is seen, scale bar is 5 nm. (c) Atomic resolution STEM-HAADF image revealing the rocksalt SmS and trigonal prismatic $TaS_2$ layers, the rotation between the layer (O-T) and (O-T)' is evident, scale bar is 2 nm. The SmS and $TaS_2$ layers which are in-phase to the electron beam focus correspond to (O-T) and those are in defocus correspond to (O-T)' orientation. (d and e) Atomic-resolution images from the area marked in image (c), projections of atomic models of double hexagonal $TaS_2$ layers and distorted rocksalt SmS are overlaid on the STEM image.*

maps overlaid on the STEM image are displayed in **Fig. 2**d-e. The STEM-EDS confirms that Sm and Ta are in antiphase relationship with each other. Since the sulfur atoms are coordinated to both samarium and tantalum atoms, the sulfur maps show a uniform distribution due to channeling phenomena in the vicinity of the heavier Ta und Sm atomic helices and do not yield any extra information here.

To understand the structural details further, nanotubes were sliced into thin lamella using a dual-beam focused ion beam (FIB) microscope and transferred onto a TEM grid. **Fig. 3**a shows a low-magnification STEM-ADF image of one such cross-section (the tube diameter is around 500 nm). A magnified image in **Fig. 3**b shows an edge dislocation and adjacent to it, a misfit structure with double layer periodicity *(O-T-T)*. It is believed that the two features occur in the vicinity to each other due to strain fields induced by the dislocation. Generally, the confined volume and curvature of the nanotubes, confer larger density of defects than in flakes.[37] Moreover, the fact that each layer in the MLC nanotube contains a different number of atoms, induces strain, which can be relaxed via defect formation. **Figs. 3**c-e show high-magnification STEM-BF images of a portion of the lamella. Indeed the top exploded area includes three such repeating *(O-T-T)* units (**Fig. 3**d). The repeating two $TaS_2$ layers appear in trigonal prismatic coordination, i.e. the 2H polytype arrangement. The rotation of 30° in the (*O-T-T*) arrangement is also evident, i.e. $TaS_2$ <10.0>/SmS<100> and $TaS_2$ <01.0>/SmS<110>. The fogging of some of the MLC layers in the HRSTEM images can be ascribed to the stacking faults, i.e. rotation of the (*O-T*) pair with respect

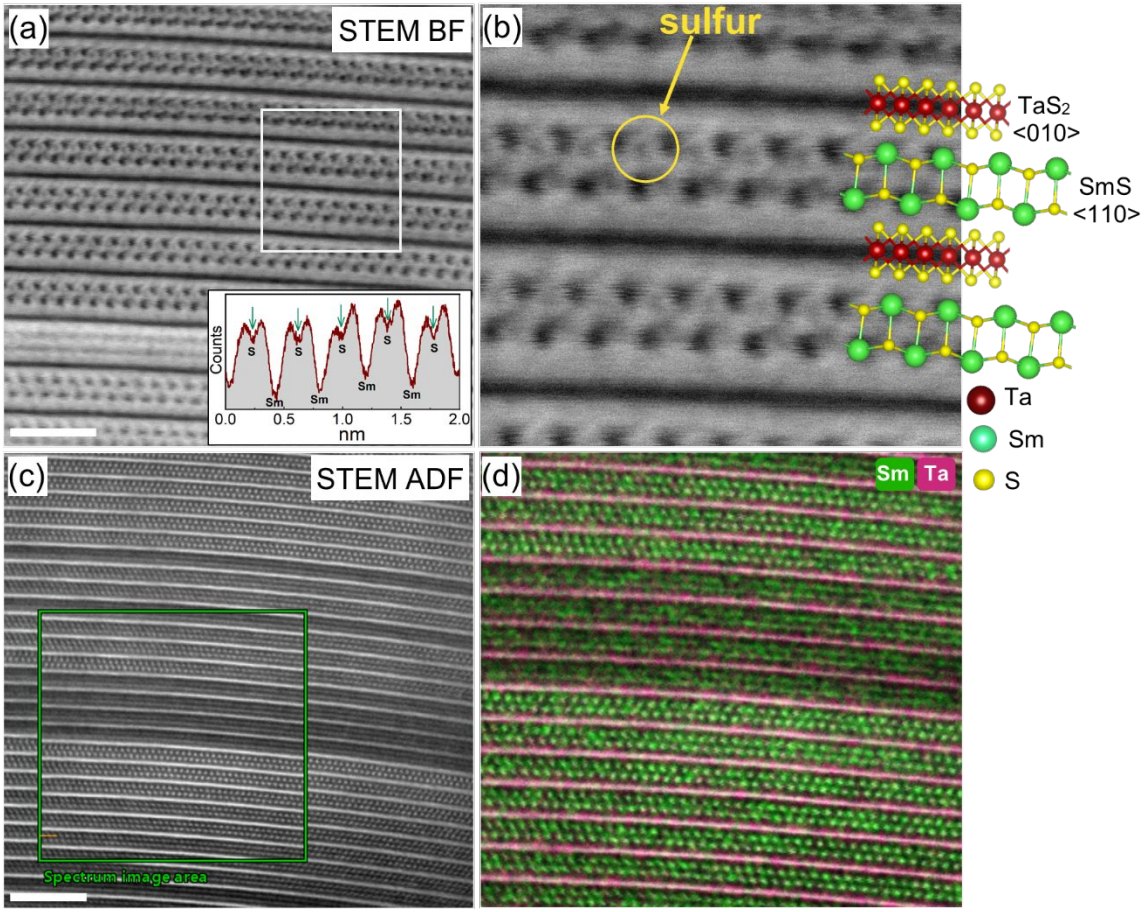


***Fig 4.*** *(a) Atomic resolution HR-STEM-BF image of a portion of the nanotube lamellae, a magnified image in (b) succinctly reveal the sulfur atoms adjacent to samarium atoms in the rock salt unit. The intensity profile is drawn from one of the SmS layers shown in the inset of (a) and it shows clear modulation of S and Sm, scale bar 2 nm. (c-d) STEM-ADF and corresponding STEM-EDS analyses of $(SmS)_{1.19}TaS_2$ nanotube lamellae. EDS mapping shows the clear antiphase correlation between Sm and Ta atoms, scale bar 5 nm. Sulfur atoms were distributed uniformly across the lamellae and are presented in the SI, Fig S6.*

to the (*O-T*)' or (*O-T-T*) and (*O-T-T*)' layers. The different crystallographic orientation of the two pairs leads to a small scattering of the incoming electron beam and blurring of the TEM image. On

the other hand, the ordered structure from other portions of the lamellae consists of purely (*O-T*) superstructures (**Figs. 3**e and **S5**), but the orientation of the layers varies from one pair to another. This observation reinforces the proposition that the (*O-T-T*) superstructure in this lamella indeed resulted from the defects formed by the SmS layer. Schematic rendering of the SmS <110> and $TaS_2$ <01.0> atomic models corresponds very well to the underlying STEM-BF image.

**Figs. 4** a, b and **Fig. S5** show HR-STEM-BF images and exploded views of a lamella from a different region of the same nanotube. The (*O-T*) superstructure order is strictly followed, extended over many layers. Since the SmS layer is oriented along <110>, the Sm and S atoms in the rocksalt structure are skewed and are therefore clearly visible in a magnified STEM-BF image (**Figs. 4**b). The intensity profile drawn from one of the SmS layers (insert of **Fig 4**a**)** reveals clear modulation of the S and Sm atoms. Note that since the rocksalt structure is distorted, the samarium and sulfur atoms do not share a common plane, i.e. the sulfur atoms are displaced towards the center of the SmS subunit. The high-resolution STEM-EDS images (**Fig. 4**d and **S6**) show that the two Sm and Ta layers are in antiphase relationship with each other. The even sulfur distribution on the entire lattice is evident (see **Fig. S6a**). The intensity profiles of the EDS chemical maps presented in the **Fig. S6**b show two Sm atomic layers (of the rocksalt unit) in between the Ta layers and their periodic modulation. The EDS sulfur profile reveals two atomic layers of trigonal prismatic coordinated sulfur adjacent to the Ta atomic layer, and the sulfur from SmS layers are also distinguishable from that of the $TaS_2$ layer. No indication for any oxide formation in the core of the nanotube was observed. The HR-STEM and STEM-EDS results presented here revealed atomically each Sm, Ta, and S atoms and their position in the MLC lattice as well as their distribution, which was not available before. The Ta-S are in trigonal prismatic coordination in the hexagonal lattice while the Sm-S atoms are coordinated in a distorted rocksalt lattice with orthorhombic symmetry. Equipped with these insights, the stability of the misfit lattice gained upon charge transfer from the SmS slab to $TaS_2$ was studied by combined XPS, EELS, and XAS analyses. These analyses were further corroborated by theoretical calculations, thereby shedding light on the structure-property relationships.

$(SmS)_{1.19}TaS_2$ powder containing nanotubes and flakes was densely spread over a carbon tape and XPS spectra were collected from the sample surface. **Fig. 5** presents XPS measurements of the $(SmS)_{1.19}TaS_2$ misfit samples in comparison with 2H-$TaS_2$ flakes. The core-level Ta 4*f* spectrum of pure $TaS_2$, **Fig. 5a,** shows pronounced oxidation as evident from the high energy shoulders at ~24 and 26 eV of Ta 4*f* doublet.[47] This signal is believed to arise from the platelet edges that point upwards in the powder grains. Curve fitting details of the Ta 4*f* doublet in $TaS_2$ and $(SmS)_{1.19}TaS_2$ are presented in **Fig. S7**. Remarkably, the Ta line appears far more homogeneous in the misfit sample, which indicates that nanotubes suffer much less edge oxidation than the ($TaS_2$) platelets. The sulfur S 2*p* core-level spectra of $TaS_2$ and $(SmS)_{1.19}TaS_2$ misfit are presented in **Fig. 5b**. Co-existence of the two misfit constituents is manifested by the S 2*p* spectrum (see also SI **Fig. S8**). Here, as expected two leading sulfur chemical states are observed, attributed to S in the trigonal prismatic $TaS_2$ and the rocksalt SmS ingredients. For the reference $TaS_2$ sample, the SmS component is missing from the S 2*p* line, while other components arise due to platelet edge oxidation (see also Ta 4f line). The 3*d* core-levels of samarium, observed at 1084 (Sm $3d_{5/2}$) and 1110 eV (Sm $3d_{3/2}$), are consistent with literature reports of the $Sm^{3+}$ chemical state (see **Fig. S9**).[48] No signature of $Sm^{2+}$ at energies 1073 and 1100 eV, were observed.[48] Earlier reports of single-crystal $(SmS)_{1.19}TaS_2$ suggested $Sm^{2+}$-$Sm^{3+}$ valance fluctuation, but no evidence of that notion is seen here. Further support for this conjecture, i.e. the existence of pure $Sm^{3+}$ and the absence of

valence fluctuations, was provided by the XAS analysis (*vide infra*). Quantitative analysis of the chemical composition showed a Sm/Ta ratio of 1.12, which is slightly lower than the theoretical value- 1.19.

The XPS valence band spectra presented in **Fig. 5c** show a clear difference between the reference ($TaS_2$) and the $(SmS)_{1.19}TaS_2$ structure. The missing feature at 4-8 eV is attributed to the lack of Sm contribution. Differences at the top of the valence band, just below the Fermi energy (zero binding energy), are seen as well. The valence band spectrum of $(SmS)_{1.19}TaS_2$, exhibits broadening plus a shift of the MLC spectrum to higher binding energies compared to the pure $TaS_2$. This result suggests that the Fermi level of the misfit was 'pushed' upwards and the misfit became less *p*-type, as compared to $TaS_2$. These differences are complemented by the work function (WF) shift shown in **Fig. 5**d. Here, a clear difference in the onset of the secondary electron emission, about 270 meV in magnitude, is seen between the reference and the MLC. The latter result suggests that the WF of bulk SmS is lower than that of $TaS_2$, hence when brought into contact with $TaS_2$ (in the MLC), electron density is expected to be transferred from the SmS to the $TaS_2$ layers. Consequently, the valence band of the semiconducting SmS is partially depopulated (by charge transfer) and thus becomes conductive as well. Interestingly, the Ta $4f_{7/2}$ binding energy of the $TaS_2$-related component in the misfit compound is similar to the one in pure $TaS_2$. This fact indicates that the donated charge contributes a charge density to the Ta atoms exclusively, such that both the Fermi energy and the Ta-core levels are equally affected (see also SI).

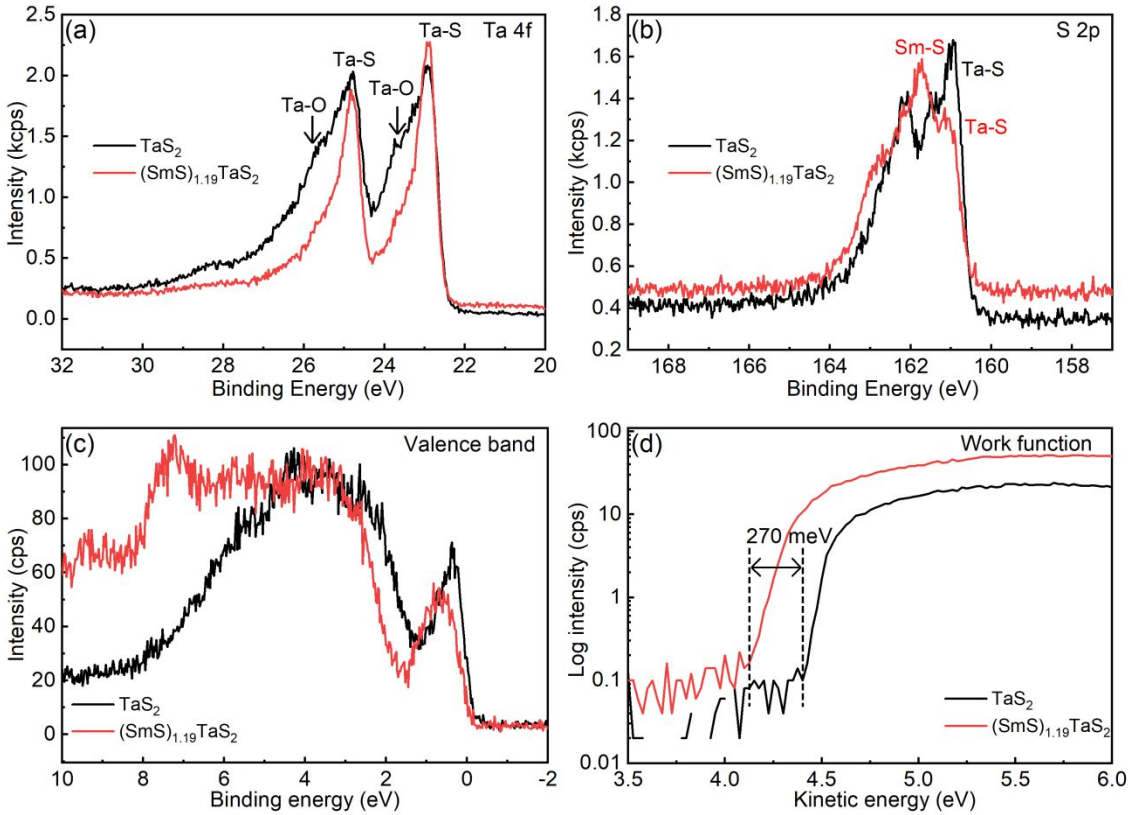


***Fig. 5**. X-ray photoelectron spectroscopic results of $TaS_2$ platelets (black) and the $(SmS)_{1.19}TaS_2$ misfit nanotubes (red). (a) the Ta 4f doublet; (b) the S 2p doublet; (c) the valence band spectral region; (d) the onset of secondary electron emission, given on a log-scale, from which the sample work function is extracted for $(SmS)_{1.19}TaS_2$ and $TaS_2$, respectively.*

Notably, XPS measurements can also provide rich information on the electrical properties of the probed samples.[49-52] In the present study, tested under extreme positive and negative charging conditions, both $TaS_2$ and SmS-$TaS_2$ are found to be very good conductors. Advantageously, these measurements, done *in-situ* in the XPS chamber, offer contactless electrical characterization. Yet, as an electrical probe, these measurements are better suited for semiconductors and insulators, yielding only limited sensitivity to the differences between the conductivity levels of metals. Notwithstanding this reservation, the conductivity of the misfit sample was found to be very similar to that of the metallic $TaS_2$ platelets. Hence, this observation suggests, in agreement with previous reports,[7] that band filling by the Sm-to-Ta charge transfer is incomplete and the metallic conductivity is preserved in both constituents of the MLC.

Monochromated low-loss EEL spectra of $TaS_2$ and $(SmS)_{1.19}TaS_2$ misfit compound are presented in **Fig. 6**. Hyperspectral data were recorded with a scanning focused probe obtaining both spatial and a high energy resolution (better than 90 meV) to resolve low-energy excitations in the near-infrared region. **Fig. 6**a displays an exemplary spectrum of a $(SmS)_{1.19}TaS_2$ nanotube, obtained as the sum of multiple spectra in a region of interest across the central part of the nanotube. The elastic contribution to the spectrum was subtracted using the mirrored left-hand tail of the zero-loss-peak (ZLP).[53] The remaining tail at the lowest energies in the inelastic part of the spectrum contains Cerenkov losses and surface losses that are flattened out here because of a large collection angle. The inelastic part of the low loss spectrum is plotted for the central part of a $(SmS)_{1.19}TaS_2$ nanotube, the edge of a $(SmS)_{1.2}TaS_2$ platelet and a 2H-$TaS_2$ platelet in **Fig. 6**b. The reference spectrum of 2H-$TaS_2$ is very distinct from those of the misfit compound: A strong transition at around 1 eV observable all across the platelets of $TaS_2$ is almost absent in the misfit layered compound. To understand the origin of this peak and the reason for its absence in the

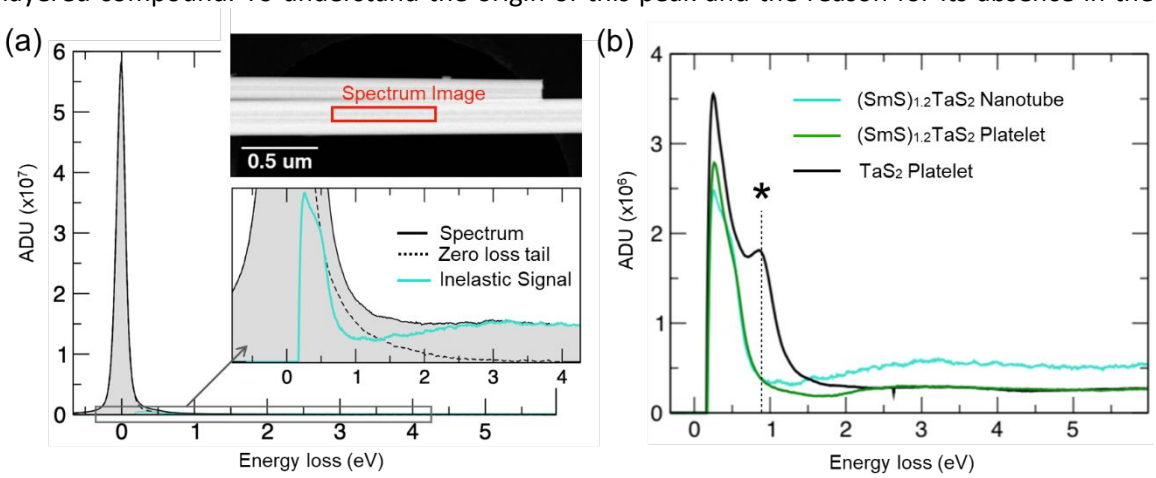


***Fig. 6**. Low-loss EEL spectra. (a) An exemplary spectrum of a $(SmS)_{1.19}TaS_2$ nanotube. The insets show an annular dark-field image of the nanotube and a magnified part of the spectrum with the extracted inelastic signal. The spectrum is a sum of spectra obtained in a region of interest (red rectangle) close to the tube axis, where the incident direction of the electron beam is close to the c-axis direction of the MLC. For background subtraction the tail of the elastic zero-loss peak was reflected from the high-energy side. (b) Inelastic part of the EEL low loss signal for three samples, the center part of a $(SmS)_{1.19}TaS_2$ nanotube (as in (a), a $(SmS)_{1.19}TaS_2$ platelet and a 2H-$TaS_2$ platelets. The platelets were transmitted in the direction of the c-axis. The strong peak at about 1 eV energy loss (marked by an asterisk) in 2H-$TaS_2$ is associated with a transition from occupied S 3p states into unoccupied Ta $5d_{z^2}$ states. The peak is absent in the MLC, in the platelet and the nanotube.*

misfit compound one has to refer to the classical dielectric formalism of the loss function.[54, 55] Accordingly, the EEL low-loss function is related to the so-called volume loss function, i.e. Im(-1/ε), where ε is the frequency-dependent dielectric function. The imaginary ($\varepsilon_2$) and real ($\varepsilon_1$) part of the frequency-dependent dielectric functions for bulk 2H-$TaS_2$, obtained from DFT calculations are presented in **Fig. S10**. A peak in $\varepsilon_2$ of 2H-$TaS_2$ just above 1 eV upon longitudinal excitation along the *c*-axis can be possibly ascribed to a transition from occupied S 3*p* states into unoccupied Ta $5d_z^2$ states above the Fermi level.

Such an S 3*p* to Ta 5*d* transition is indeed likely to apply for the ~1 eV loss in the $TaS_2$ EEL spectrum, because it does not violate the dipole selection rules. Yet, the intensity of this peak is particularly high and, therefore, the related transition is suspected to be of a significant intra-atomic character, other than inter-atomic. This transition is enabled by intra-atomic transitions between, e.g. 5*d* Ta 3/2 and 5/2 states. Remarkably, the 1 EV EELS peak is practically absent from the $(SmS)_{1.19}TaS_2$ nanotubes and platelets. This result can be attributed to an almost complete filling of the Ta $5d_z^2$ states in the misfit compound. The DFT calculations further substantiate an almost complete occupation of these Ta *d* states (*vide infra*). In agreement with the EEL data, the theoretical dielectric function of $(SmS)_{1.2}TaS_2$, obtained by DFT calculations does not show the excitation at about 1eV (**Fig. S10**) owing to the charge transfer from the Sm 4*f*-band to the Ta $5d_z^2$ states in the misfit compound.

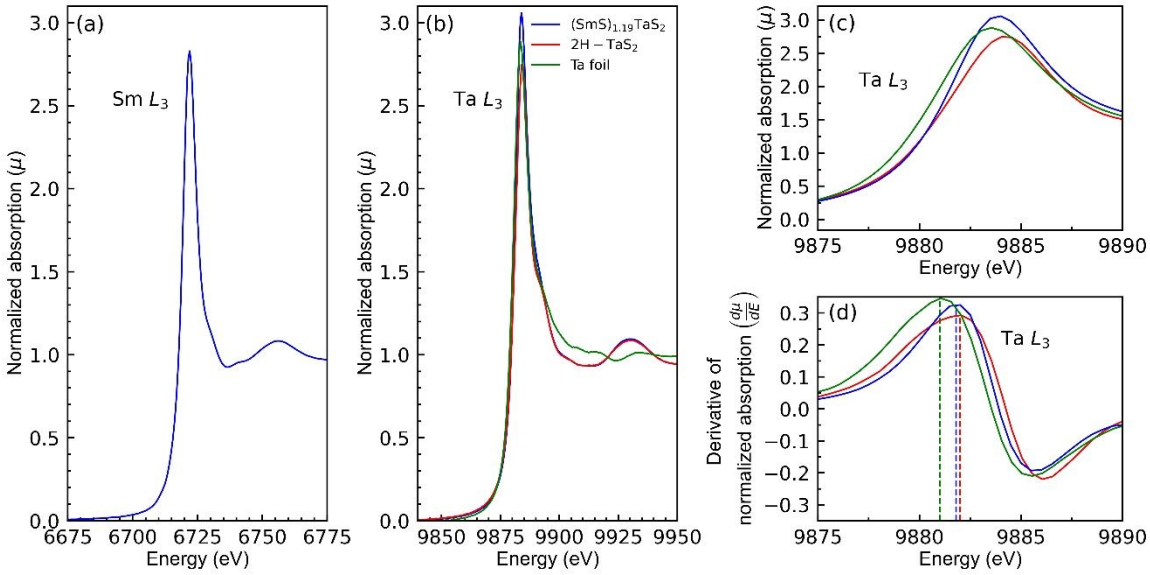


***Fig. 7.*** *XANES spectra of $(SmS)_{1.19}TaS_2$ and $TaS_2$ powders dispersed in the polymer matrix and pure (99.99 %) Ta foil collected in a transmission geometry at PETRA III P23 beamline. Spectral regions for Sm-$L_3$ (a) and Ta-$L_3$ (b, c) edges. (d) Derivative of the normalized absorption in the vicinity of Ta $L_3$ edge. XANES in (a), (b) and (c) spectra are normalized to the edge step and the energy scale is calibrated with pure Ta and Mn foils.*

Unlike the surface-sensitive XPS, XAS analysis provides the finest structural, chemical state and charge transfer insights of the bulk. **Fig. 7** shows Sm $L_3$ and Ta $L_3$ XANES spectra of $(SmS)_{1.19}TaS_2$ misfit compound (nanotube + flakes) in comparison with 2H-$TaS_2$ and Ta foil (99.99%) collected in transmission geometry. The shape of the Sm $L_3$ XANES spectrum (**Fig. 7a**) and the position of the 'white line' maxima at 6722 eV, (edge position 6719.5 eV, corresponding to 2*p* to 5*d* transition) is characteristic of $Sm^{3+}$ state.[56] No signature of $Sm^{2+}$ 'white line' in the range 6711-6713 eV was found, indicating that there is no mixed/intermediate valence state of Sm, which in turn signifies

a strong charge transfer.[56-58] This observation is in-line with the XPS and also with the literature reports.[7, 8]

The shape of the Ta $L_3$ XANES spectrum (**Fig. 7b**) resembles the 2H-$TaS_2$ spectra, and the position of the 'white line' at 9884 eV is close to that of the 2H-$TaS_2$ structures.[59, 60] However, precise examination of the 'white line' (**Fig. 7c**) or the absorption edge position from the derivative of the normalized absorption (**Fig. 7d**), shows that there is a small shift between 2H-$TaS_2$ (9881.8 ± 0.1 eV) and the $(SmS)_{1.19}TaS_2$ (9882 ± 0.1eV) Ta $L_3$ edges. It is known that the position of the Ta $L_3$ edge depends on the valence state of Ta: the higher the valence (oxidation state) the stronger Ta $L_3$ edge shifts towards higher X-ray energies.[61, 62] **Fig. 7d** shows that the position of Ta $L_3$ edge of pure Ta foil has slightly lower value (oxidation state = 0, edge position 9881 ± 0.1) than that of $TaS_2$ and $(SmS)_{1.19}TaS_2$. The small difference between the $L_3$ edges of $TaS_2$ and $(SmS)_{1.19}TaS_2$ (0.2± 0.1 eV) can-not be over-interpreted, since some tantalum-oxide may have been occurred on the surface of the tubes (flakes). The $(SmS)_{1.19}TaS_2$ Ta $L_3$ 'white' line intensity (3.01 ± 0.01), which corresponds to the transition from the 2*p* core level to unoccupied Ta 5*d* states ($d_z^2$ band), is higher than the 'white line' intensity value measured for pristine 2H-$TaS_2$ (2.75 ± 0.01).[59, 63] Interestingly, the intercalation of pristine 2H-$TaS_2$ by pyridine[59] or hydrazine[63] increases the intensity of the 'white line' up to the value of 2.5 and 2.9, respectively. In the case of $(SmS)_{1.19}TaS_2$, the charge transfer from SmS to $TaS_2$ would lead to a similar increase in the white line intensity of Ta $L_3$ in comparison with pristine 2H-$TaS_2$. In general, XAS investigations show that the white line intensity grows with electron-donating intercalates and diminishes with electron-withdrawing intercalates.[59, 63] The fundamental reason for such a change is yet to be understood.

**Density Functional Theory (DFT)**

DFT calculations were employed to get an insight into the electronic structure of the SmS-$TaS_2$ MLC and to compare it to the parent SmS and $TaS_2$ phases. As a misfit model, the approximant $(SmS)_{1.20}TaS_2$ was chosen, in which a supercell included one SmS slab (12 SmS units) and one $TaS_2$ layer (10 $TaS_2$ units). A preliminary geometry optimization yielded the lattice parameters for misfit as $a$ = 17.08 Å, $b$ = 5.79 Å and $c/2$ = 11.53 Å. The in-plane parameters fitting for the $TaS_2$ sub-lattice were close to that of bulk 2H-$TaS_2$ (calc. $a$ = 3.35 Å). On the other hand, the SmS sublattice showed a slight contraction compared to the bulk compound. Little peculiarity can be observed in the distortion of the SmS slab within SmS-$TaS_2$ misfit, when compared to the LaS slab within the LaS-$TaS_2$ misfits studied earlier.[26] The angles of the S-Sm-S configurations in this slab vary in the range 80-89° with the S atoms retracting into the slab, which is in agreement with the atom positions in the atomic-resolution STEM-BF images (see ball-and-stick model in **Fig. 8**).

While the calculations within Local Density Approximation or Generalized Gradient Approximation (LDA or GGA) ascribe a semi-metallic character for bulk SmS, the present LDA+U calculations describe this compound as a semiconductor with direct Γ-Γ transition type and a fundamental band gap of 0.69 eV (**Fig. 8**a, and **Fig. S11**). The latter is consistent with the scattering in the available experimental and theoretical data. The experimentally reported gap is 0.15 eV[64] or 0.4 eV[65] whereas the calculated values are 0.25 eV [65] or 0.71 eV.[66] The bandgap edges arise from the highly intense and strongly localized band of occupied Sm4*f*-states and from the shallow band of unoccupied Sm6*s*-states. The valence band of the occupied S3*p*-states is found at 2.5-5.5

eV below the top of the Sm4*f*-band. In general, such a DOS profile characterizes SmS as a lattice with a highly ionic character. The nominal oxidation states of the elements are $Sm^{2+}$ and $S^{2-}$ and the Sm4*f* states do not participate in the chemical bonding. Remarkably, the occupation and composition of the conduction band in the electronic structure of SmS is different from that of the isostructural LaS. In the latter, the Fermi level is hosted at a shallow band of La5*d*-states as shown in **Fig. S11**.

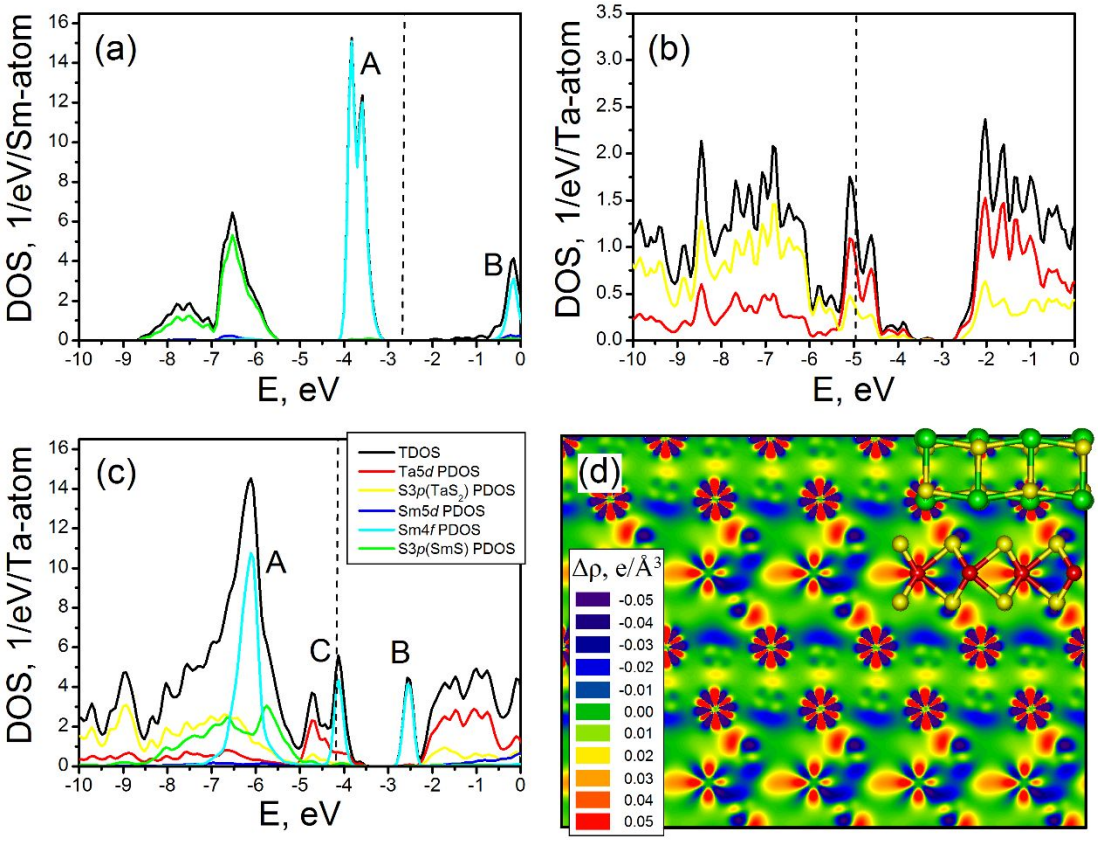


**Fig. 8.** *Electronic densities-of-states (DOSs) for bulk fcc-SmS (a) 2H-$TaS_2$ (b) and misfit $(SmS)_{1.20}TaS_2$ (c). Fermi level is drawn as a dashed line. Panel (d) depicts the electronic density redistribution map after the $(SmS)_{1.20}TaS_2$ crystal assembly from SmS slabs and $TaS_2$ monolayers. Sm, S and Ta atoms of the ball-and-stick models are painted in green, yellow and red, respectively. Corresponding spin-resolved band structures are plotted on **Fig. S11**. DFT LDA+U calculations.*

According to the present and also earlier calculations, bulk 2H-$TaS_2$ is a metal, where the Fermi level is hosted at the band of well-localized Ta5$d_{z^2}$-states, see **Fig. 8**b. The wide valence band is composed of a mixture of dominating S3*p*- and secondary Ta5*d*-states responsible for the covalent Ta-S bonding. The wide conduction band is dominated by the Ta5*d*- and secondary S3*p*-states and is separated from the Ta5$d_{z^2}$-band by a gap of ~0.5 eV. The latter reflects the well-documented tendency of $TaS_2$ to act as an acceptor within misfit compounds, (almost) filling the 5$d_{z^2}$-band similar to 4$d_{z^2}$- or 5$d_{z^2}$-bands in the semiconducting $MoS_2$ or $WS_2$.

In analogy with the (La,Y)S-$TaS_2$ misfits studied in the past[25], $(SmS)_{1.19}TaS_2$ possesses a metal-like character in the framework of LDA+U calculations (**Fig. 8**c). Here, the metallic properties of SmS-$TaS_2$ arise due to the charge transfer from Sm4*f*- to Ta5$d_{z^2}$-states within individual SmS and $TaS_2$ components acting as the donor and the acceptor of electron density, respectively. The absolute

value of the Fermi level in SmS-$TaS_2$ is found to be in-between the Fermi levels of the parent binary compounds (**Fig. S11**). The calculated effective charge on Sm atoms increases from +0.53 e in SmS to the average value of +0.81 e in $(SmS)_{1.20}TaS_2$, while the effective magnetic moments on all these atoms decrease from 6.97 $\mu_B$ to 6.49 $\mu_B$ on the average, respectively.

In contrast to (La,Y)S-$TaS_2$ misfits, the DOS profile of SmS-$TaS_2$ misfit can not be assembled from the DOS profiles for the individual SmS and $TaS_2$ in a simplified rigid-band model. The charge transfer in SmS-$TaS_2$ is accompanied by remarkable reorganization of the Sm4*f*-states compared to the pristine SmS compound (see bands A, B, C in **Fig. 8**a, c). The Fermi level is hosted at the shoulder of a Sm4*f*-band (C-band), which is split-off from the main occupied Sm4*f*-band (A-band). This new C-band is also well localized and appears in the pristine SmS compound, nearly in the middle between occupied A-band and unoccupied B-band. Noteworthy, the A-band in SmS-$TaS_2$ is aligned with both the occupied S3*p*-band of SmS and the occupied S3*p*-band of $TaS_2$, which may point to additional strengthening of Sm-S bonding both within the SmS layer and at the SmS||$TaS_2$ interface. Indeed, mapping the electron density redistribution within $(SmS)_{1.20}TaS_2$ unveils not only an enhancement of electron density at the Ta atoms (four-lobed patterns of Ta5*d*-orbitals in **Fig. 8**d), but also a charge redistribution within the Sm atoms (six-lobed patterns of Sm4*f*-orbitals). Furthermore, an enhancement of electron density between the Sm atoms and the S atoms of $TaS_2$ is visible, which is responsible for the rise of a new coordinate Sm-S bonding (red "blobs" between Sm and S). A slight enhancement of the electron density between Sm and S atoms within the SmS unit can be also observed.

To complement the data of low-loss EEL spectroscopy, the frequency-dependent dielectric functions $\varepsilon(\omega) = \varepsilon_1(\omega) + i\varepsilon_2(\omega)$, where $\varepsilon_1(\omega)$ and $\varepsilon_2(\omega)$ are the real and imaginary parts of the function, respectively, have been calculated using the same pseudopotential DFT method for in-plane (xx) and out-of-plane (zz) scattering on both 2H-$TaS_2$ and $(SmS)_{1.20}TaS_2$ compounds (**Fig. S10**). The results for $TaS_2$ are in semi-qualitative agreement with the optical properties elucidated from the EELS analysis (**Fig. 6**) and more sophisticated full-potential plane-wave calculations.[67] The origin of the signal at ~1 eV in the inelastic part of the low-loss EEL spectrum along *c*-axis of $TaS_2$ and the corresponding maximum of $\varepsilon_2^{zz}(\omega)$ function at ~1.5 eV in the calculations, are related to the electron transfer into the half-filled Ta5$d_{z^2}$-band, see **Fig. S10**a. Contributions to these transitions arise from the S 3*p* and Ta 5*d* states (**Fig. 8**b), noting that both of them are dipole-allowed ($\Delta j=\pm1$) transitions. The real part of the dielectric function, $\varepsilon_1$, influences as well the 1 eV region. Yet, in common to all related transitions, the role of the empty Ta 5$d_{z^2}$ states is dominant. In contrast, for the misfit structure, the ~1 eV region is modified significantly, due to the charge transfer discussed above. Accordingly, the dielectric function calculated for $(SmS)_{1.20}TaS_2$ confirms the disappearance of the EEL signal from the ~1 eV regime, when applied along the *c*-axis of the MLC (**Fig. S10**b).

**Magnetic measurements**

The ac susceptibility measured at frequencies 1, 100, and 1000 Hz and zero dc magnetic field show a strong diamagnetic signal below 3.9 K (**Fig. 9a**), indicating that $(SmS)_{1.19}TaS_2$ undergoes superconducting transition below 5 K. This transition temperature is appreciably higher than that occurring in 2H-$TaS_2$ (0.63 K).[45] The presence of diamagnetic signals is also verified by zero-field cooled dc magnetization measured at a magnetic field of 20 Oe (**Fig. 9a**, inset) and the transition temperature obtained by both ac and dc measurements is in excellent agreement. The low-temperature ac susceptibility shows a large volume fraction ~45%, of the superconducting phase, indicating the bulk superconducting in nature. The isothermal magnetization, M(H), measured at 2 K shows butterfly-shaped hysteresis loops (**Fig. 9b**) possibly associated with Type-II

superconductivity.[68] The observed behavior was verified three times for $(SmS)_{1.19}TaS_2$ sample prepared in different batches. No superconductivity transition was observed in the magnetic measurements of GdS-$TaS_2$ tubes and flakes, which were prepared in a similar way (see **Fig. S12**). The iso-field, iso-thermal magnetic and ac susceptibility measurements show that GdS-$TaS_2$ ordered antiferromagnetically at temperate 7K (**Fig. S12**).

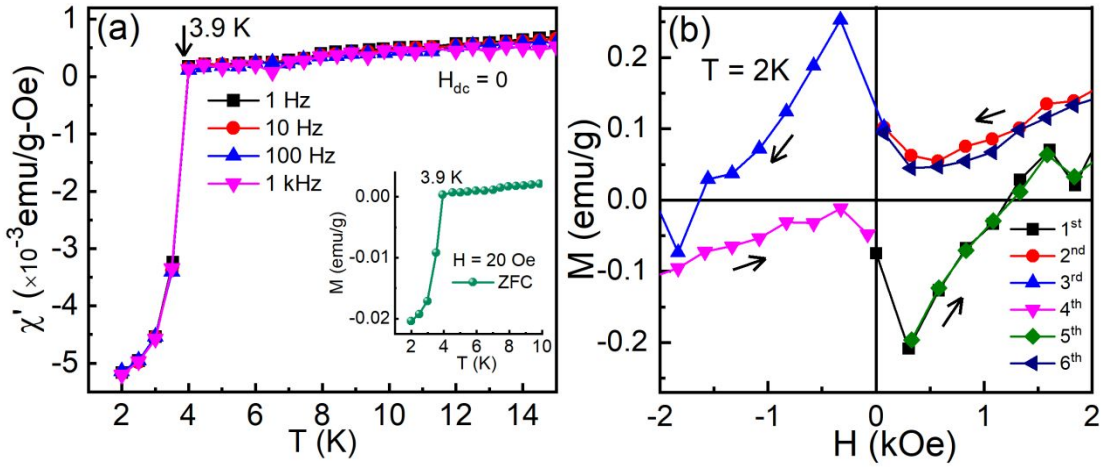


***Fig. 9.*** *Temperature-dependent magnetic susceptibility of $(SmS)_{1.19}TaS_2$ MLC, (a) Real part of the ac magnetic susceptibility measured at frequencies, f = 1, 10, 100 and 1000 Hz and $H_{dc}$ = 0. Inset in (a) shows zero-field cooled dc magnetization as a function of temperature measured at $H_{dc}$ = 20 Oe. (b) Zero field cooled isothermal magnetization measured at T = 2K. The hysteresis loops were carried out as 0 → +10 (first cycle)→ –10 (second and third cycles)→ +10 (fourth and fifth cycles)→ 0 kOe (sixth cycle). Only the part of hysteresis loops was shown for clarity.*

Charge density waves (CDW) and superconductivity (SC) co-exist in 2H-$TaS_2$.[69] It is well understood that the intercalation of alkali metals such as Li/Na and pyridine would enhance the superconducting transition temperatures and suppress the CDW transition.[69] The intercalation of small quantities of Li or pyridine in 2H-$TaS_2$ was shown to enhance the SC critical temperature- $T_c$ from 0.8 K to 3.5 K.[69] A similar effect can be anticipated in misfit compounds, whereby the enhancement in $T_c$ of $(SmS)_{1.19}TaS_2$ compared to pure $TaS_2$ is reminiscent of the strong charge transfer from SmS to $TaS_2$. The superconductivity in a series of MLCs was studied before using heat capacity and magnetic susceptibility analyses.[70] The authors did not find any superconductivity in LaS-$NbS_2$ and SmS-$NbS_2$, which was attributed to the strong charge transfer between the layers and the stronger polar coupling between the layers, compared to other MLCs. Note that no evidence for the presence of pure tantalum impurities ($T_c$= 4.4 K) was obtained by any of the techniques used in this study. Magnetic susceptibility of SmS-$TaS_2$ under relatively high magnetic fields (0.875 T), and did not exhibit a superconductivity transition.[7] The $\chi^{-1}$ *vs* temperature curve in the interval 100 K < T < 300 K shows good agreement (R-factor = 0.99987) with the Curie-Weiss equation (**Fig. S13**), the derived Curie constant is C = 0.0627(6) $cm^3$ K $mole^{-1}$. The effective magnetic moment is equal to $\mu_{eff}$ = 0.71 $\mu_B$ while the calculated value of $\mu_{eff}$ for $Sm^{3+}$ is 0.84 $\mu_B$.[71] Thus samarium in $(SmS)_{1.2}TaS_2$ MLC exists in $Sm^{3+}$ state with $4f^5$ ($^6H_{5/2}$) electronic configuration.

**Transport measurements**

Transport properties of individual LaS-$TaS_2$ nanotubes were recently reported.[44] In support of the DFT calculations, the LaS-$TaS_2$ nanotubes were found to be semimetallic. Given the fact that the Sm-based MLC is chemically more stable than the LaS-$TaS_2$ and the improved handling of the

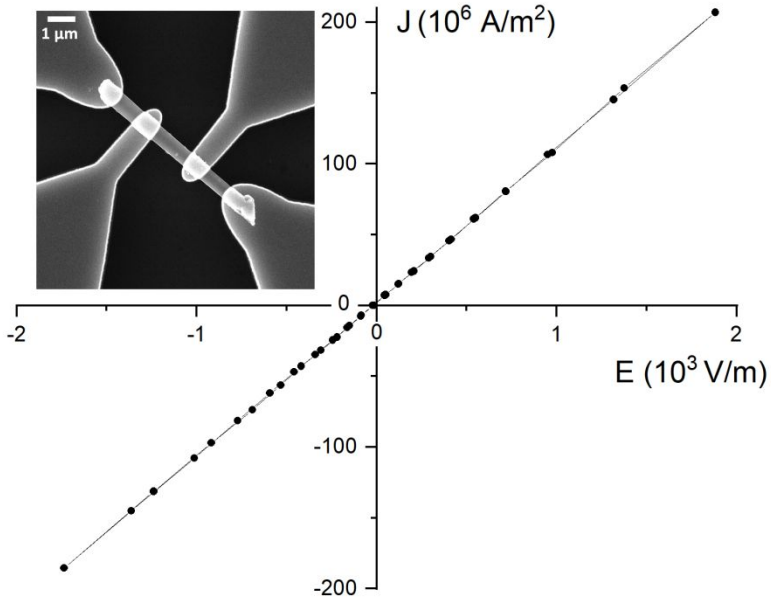


***Fig. 10**. A typical I-V curve of a single $(SmS)_{1.19}TaS_2$ nanotube (550 nm in diameter and 7 µm long), giving resistivity $\rho = 0.92 \times 10^{-3} \Omega\square\mathrm{cm}$. Several devices of this kind were prepared, exhibiting resistivities between $(0.40 - 0.95) \times 10^{-3}\ \Omega\square\mathrm{cm}$. The inset is an SEM image of nanotube (in the middle) with four contact probes fabricated using EBL, showing the geometry of devices used for (room temperature) electrical transport measurements.*

nanotubes, surface oxidation of the nanotubes were generally less of an issue here. Several devices of this kind were prepared and measured (**Fig. 10**). The specific resistivities derived from the measurements are in the range of $(0.40 - 0.95) \times 10^{-3}\ \Omega\square\mathrm{cm}$. These resistivity values are similar to the room temperature resistivity of bulk 2H-$TaS_2$, which is on the order of $5\times10^{-3}\ \Omega\square$ cm.[72] In fact these values are comparable to the values reported in Ref. 7. The somewhat counterintuitive low resistivity of SmS-$TaS_2$ nanotubes, which is comparable to that of 2H-$TaS_2$ flakes can be possibly attributed to their quasi-1D structure, which leads to a reduced scattering of the charges. Preliminary cathodoluminescence (CL) measurements of individual nanotubes in cryogenic temperatures (-150 K) were carried-out within the SEM. The CL spectra revealed *f-f* luminescence with a peak at 695 nm (see **Fig. S14**), which were absent in the background. The 695 nm luminescence peak has been previously assigned to $Sm^{2+}$ and is attributed to the local reduction of $Sm^{3+}$ by the electron beam.[73]

**Conclusions**

Herein, the structure and some physical properties of nanotubes and flakes formed from the misfit layered compound $(SmS)_{1.2}TaS_2$ were studied. High-resolution transmission electron microscopy (HR-STEM) was used to shed light on the structure of the nanotubes in detail. Their cross-sectional lamella were prepared and studied via HR-STEM providing unprecedented resolution of the lattice-atoms in the nanotube. In particular, the trigonal prismatic arrangement of the 2H-$TaS_2$ was clearly visible. X-ray photoelectron spectroscopy and X-ray absorption and electron energy loss spectroscopy analyses coupled with density functional theory calculations

indicated that strong charge transfer from the samarium 4*f* level to the $5d_z^2$ levels in $TaS_2$ leads to the partial filling of these energy levels. This charge transfer has several implications. First, the Sm atom is present as $Sm^{3+}$ valence state in the MLC lattice. Also, the SmS-$TaS_2$ exhibits a comparable conductivity to bulk 2H-$TaS_2$, which is vindicated through four probe transport measurements. Finally, the charge transfer suppresses the charge density wave phase of $TaS_2$, promoting thereby the superconductivity of this MLC with $T_c$ of 3.8-4.4 K compared to 0.8 K for bulk 2H-$TaS_2$. This study sheds new light on the structure-properties relations in MLC and their nanotubes in particular. In particular, the present study demonstrates that Ln-based MLC nanotubes are likely to exhibit intriguing 1D quantum physical phenomena at cryogenic temperatures.

**Acknowledgements**

This work was partially supported by the Israel Science Foundation grant No. 339/18 (Internal grant No. 120924) (RT). The following foundations are acknowledged: Perlman Family Foundation; the Kimmel Center for Nanoscale Science Grant No. 43535000350000; the Irving and Cherna Moskowitz Center for Nano and Bio-Nano Imaging. CzechNanoLab project LM2018110 funded by MEYS CR is gratefully acknowledged for the financial support of the measurements and sample fabrication at CEITEC Nano Research Infrastructure. This work was partially supported by Ceitec Nano+ (CZ.02.01/0.0./.0.0./16_013/0001728 under Program OPVVV) and the Horizon 2020 Research and Innovation Programme under Grant Agreement 810626 (SINNCE). Work at Ames Laboratory was supported by the Materials Sciences and Engineering Division of the Office of Basic Energy Sciences, Office of Science of U. S. Department of Energy. Ames Laboratory is operated for the U.S. DOE by Iowa State University of Science and Technology under Contract No. DE-AC02-07CH11358. A part of work at Buffalo State was supported by the faculty startup fund from the Dean's Office, School of Arts and Sciences, State University of New York (SUNY), Buffalo State. We acknowledge DESY (Hamburg, Germany), a member of the Helmholtz Association HGF, for the provision of experimental facilities for XAS studies. Parts of this research were carried out at PETRA III, P23 "In-situ and X-ray imaging beamline".

**Supporting Information**

Experimental and characterization details, computation details, XRD, HR-STEM, STEM-EDS, magnetic measurements, electrical characterization, frequency-dependent dielectric function, Band structure of LaS-$TaS_2$ and SmS-$TaS_2$, magnetic susceptibility fitting of $\chi$(T) Curie-Weiss equation and cathodoluminescence.

**References**

1. Makovicky, E.; Hyde, B. G., Non-commensurate (misfit) layer structures. In *Inorganic Chemistry; Structure and Bonding*, Springer Berlin Heidelberg: 1981; Vol. 46, pp 101-170.

2. Williams, T. B.; Hyde, B. G., Electron microscopy of cylindrite and franckeite. *Physics and Chemistry of Minerals* **1988,** 15, (6), 521-544.

3. Wiegers, G. A.; Meerschaut, A., Incommensurate Sandwiched Layered Compounds. In Materials Science Forum. In *Materials Science Forum*, Meerschaut, A., Ed. Trans Tech Publications: Pfaffikon, Switzerland: 1992; Vol. 100-101, pp 223-272.

4. Wiegers, G. A.; Meerschaut, A., Structures of misfit layer compounds $(MS)_nTS_2$ (M= Sn, Pb, Bi, rare earth metals; T=Nb, Ta, Ti, V, Cr; 1.08<n<1.23). *J. Alloys Compd.* **1992,** 178, (1), 351-368.

5. Oosawa, Y.; Gotoh, Y.; Akimoto, J.; Tsunoda, T.; Sohma, M.; Onoda, M., Three Types of Ternary Selenides with Layered Composite Crystal Structures Formed in the Pb-Nb-Se System. *Jpn. J. Appl. Phys.* **1992,** 31, (Part 2, No. 8A), L1096-L1099.

6. Wiegers, G. A., Misfit layer compounds: Structures and physical properties. *Prog. Solid State Chem.* **1996,** 24, (1), 1-139.

7. Wiegers, G. A.; Meetsma, A.; Haange, R. J.; de Boer, J. L., Structure, electrical transport and magnetic properties of the misfit layer compound $(SmS)_{1.19}TaS_2$ "$SmTaS_3$". *Journal of the Less Common Metals* **1991,** 168, (2), 347-359.
8. Suzuki, K.; Enoki, T.; Bandow, S., Electronic properties and valence state of Sm in $(SmS)_{1.19}TaS_2$. *Phys. Rev. B 48* **1993,** 48, (15), 11077-11085.
9. Lin, Q.; Smeller, M.; Heideman, C. L.; Zschack, P.; Koyano, M.; Anderson, M. D.; Kykyneshi, R.; Keszler, D. A.; Anderson, I. M.; Johnson, D. C., Rational Synthesis and Characterization of a New Family of Low Thermal Conductivity Misfit Layer Compounds $[(PbSe)_{0.99}]_m(WSe_2)_n$. *Chem. Mater.* **2010,** 22, (3), 1002-1009.
10. Merrill, D. R.; Moore, D. B.; Bauers, S. R.; Falmbigl, M.; Johnson, D. C., Misfit Layer Compounds and Ferecrystals: Model Systems for Thermoelectric Nanocomposites. *Materials* **2015,** 8, (4), 2000-2029.
11. Li, Z.; Bauers, S. R.; Poudel, N.; Hamann, D.; Wang, X.; Choi, D. S.; Esfarjani, K.; Shi, L.; Johnson, D. C.; Cronin, S. B., Cross-Plane Seebeck Coefficient Measurement of Misfit Layered Compounds $(SnSe)_n(TiSe_2)_n$ (n = 1,3,4,5). *Nano Lett.* **2017,** 17, (3), 1978-1986.
12. Yin, C.; Liu, H.; Hu, Q.; Tang, J.; Pei, Y.; Ang, R., Texturization-Induced In-Plane High-Performance Thermoelectrics and Inapplicability of the Debye Model to Out-of-Plane Lattice Thermal Conductivity in Misfit-Layered Chalcogenides. *ACS Appl. Mater. Interfaces* **2019,** 11, (51), 48079-48085.
13. Putri, Y. E.; Wan, C.; Wang, Y.; Norimatsu, W.; Kusunoki, M.; Koumoto, K., Effects of alkaline earth doping on the thermoelectric properties of misfit layer sulfides. *Scr. Mater* **2012,** 66, (11), 895-898.
14. Rouxel, J.; Moeelo, Y.; Lafond, A.; DiSalvo, F. J.; Meerschaut, A.; Roesky, R., Role of Vacancies in Misfit Layered Compounds: Case of the Gadolinium Chromium Sulfide Compound. *Inorg. Chem.* **1994,** 33, (15), 3358-3363.
15. Lin, Q.; Heideman, C. L.; Nguyen, N.; Zschack, P.; Chiritescu, C.; Cahill, D. G.; Johnson, D. C., Designed Synthesis of Families of Misfit-Layered Compounds. *Eur. J. Inorg. Chem.* **2008,** 2008, (15), 2382-2385.
16. Moore, D. B.; Beekman, M.; Disch, S.; Johnson, D. C., Telluride Misfit Layer Compounds: $[(PbTe)_{1.17}]_m(TiTe_2)_n$. *Angew. Chem. Int. Ed.* **2014,** 53, (22), 5672-5675.
17. Panchakarla, L. S.; Radovsky, G.; Houben, L.; Popovitz-Biro, R.; Dunin-Borkowski, R. E.; Tenne, R., Nanotubes from Misfit Layered Compounds: A New Family of Materials with Low Dimensionality. *J. Phys. Chem. Lett.* **2014,** 5, (21), 3724-3736.
18. Bernaerts, D.; Amelinckx, S.; Van Tendeloo, G.; Van Landuyt, J., Microstructure and formation mechanism of cylindrical and conical scrolls of the misfit layer compounds $PbNb_nS_{2n+1}$. *J. Cryst. Growth* **1997,** 172, (3), 433-439.
19. Gómez-Herrero, A.; Landa-Cánovas, A. R.; Hansen, S.; Otero-Díaz, L. C., Electron microscopy study of tubular crystals $(BiS)_{1+\delta}(NbS_2)_n$. *Micron* **2000,** 31, (5), 587-595.
20. Qin, F.; Shi, W.; Ideue, T.; Yoshida, M.; Zak, A.; Tenne, R.; Kikitsu, T.; Inoue, D.; Hashizume, D.; Iwasa, Y., Superconductivity in a chiral nanotube. *Nat Commun* **2017,** 8, (1), 14465.
21. Zhang, Y. J.; Ideue, T.; Onga, M.; Qin, F.; Suzuki, R.; Zak, A.; Tenne, R.; Smet, J. H.; Iwasa, Y., Enhanced intrinsic photovoltaic effect in tungsten disulfide nanotubes. *Nature* **2019,** 570, (7761), 349-353.
22. Hong, S. Y.; Popovitz-Biro, R.; Prior, Y.; Tenne, R., Synthesis of $SnS_2$/SnS Fullerene-like Nanoparticles: A Superlattice with Polyhedral Shape. *J. Am. Chem. Soc.* **2003,** 125, (34), 10470-10474.
23. Ohno, Y., Lamellar and filament-like crystals of misfit-layer compounds containing (Sm, Ta, S) and (Pb, Bi, Nb, S) elements. *J. Solid State Chem.* **2005,** 178, (5), 1539-1550.

24. Serra, M.; Arenal, R.; Tenne, R., An overview of the recent advances in inorganic nanotubes. *Nanoscale* **2019,** 11, (17), 8073-8090.
25. Hettler, S.; Sreedhara, M. B.; Serra, M.; Sinha, S. S.; Popovitz-Biro, R.; Pinkas, I.; Enyashin, A. N.; Tenne, R.; Arenal, R., YS-$TaS_2$ and $Y_xLa_{1-x}S$-$TaS_2$ ($0 \leq x \leq 1$) Nanotubes: A Family of Misfit Layered Compounds. *ACS Nano* **2020,** 14, (5), 5445-5458.
26. Radovsky, G.; Popovitz-Biro, R.; Lorenz, T.; Joswig, J.-O.; Seifert, G.; Houben, L.; Dunin-Borkowski, R. E.; Tenne, R., Tubular structures from the LnS–$TaS_2$ (Ln = La, Ce, Nd, Ho, Er) and LaSe–$TaSe_2$ misfit layered compounds. *J. Mater. Chem. C* **2016,** 4, (1), 89-98.
27. Serra, M.; Stolovas, D.; Houben, L.; Popovitz-Biro, R.; Pinkas, I.; Kampmann, F.; Maultzsch, J.; Joselevich, E.; Tenne, R., Synthesis and Characterization of Nanotubes from Misfit $(LnS)_{1+y}$TaS2 (Ln=Pr, Sm, Gd, Yb) Compounds. *Chem. Eur. J.* **2018,** 24, (44), 11354-11363.
28. Jayaraman, A.; Bucher, E.; Dernier, P. D.; Longinotti, L. D., Temperature-Induced Explosive First-Order Electronic Phase Transition in Gd-Doped SmS. *Phys. Rev. Lett.* **1973,** 31, (11), 700-703.
29. Hall, J.; Ehlen, N.; Berges, J.; van Loon, E.; van Efferen, C.; Murray, C.; Rösner, M.; Li, J.; Senkovskiy, B. V.; Hell, M.; Rolf, M.; Heider, T.; Asensio, M. C.; Avila, J.; Plucinski, L.; Wehling, T.; Grüneis, A.; Michely, T., Environmental Control of Charge Density Wave Order in Monolayer 2H-$TaS_2$. *ACS Nano* **2019,** 13, (9), 10210-10220.
30. Rogers, E.; Smet, P. F.; Dorenbos, P.; Poelman, D.; van der Kolk, E., The thermally induced metal–semiconducting phase transition of samarium monosulfide (SmS) thin films. *J. Phys.: Condens. Matter* **2009,** 22, (1), 015005.
31. Sousanis, A.; Smet, P. F.; Poelman, D., Samarium Monosulfide (SmS): Reviewing Properties and Applications. *Materials* **2017,** 10, (8), 953.
32. Jayaraman, A.; Narayanamurti, V.; Bucher, E.; Maines, R. G., Continuous and Discontinuous Semiconductor-Metal Transition in Samarium Monochalcogenides Under Pressure. *Phys. Rev. Lett.* **1970,** 25, (20), 1430-1433.
33. Barla, A.; Sanchez, J. P.; Haga, Y.; Lapertot, G.; Doyle, B. P.; Leupold, O.; Rüffer, R.; Abd-Elmeguid, M. M.; Lengsdorf, R.; Flouquet, J., Pressure-Induced Magnetic Order in Golden SmS. *Phys. Rev. Lett.* **2004,** 92, (6), 066401.
34. Pan, J.; Guo, C.; Song, C.; Lai, X.; Li, H.; Zhao, W.; Zhang, H.; Mu, G.; Bu, K.; Lin, T.; Xie, X.; Chen, M.; Huang, F., Enhanced Superconductivity in Restacked $TaS_2$ Nanosheets. *J. Am. Chem. Soc.* **2017,** 139, (13), 4623-4626.
35. Meetsma, A.; Wiegers, G. A.; Haange, R. J.; de Boer, J. L., Structure of 2H-$TaS_2$. *Acta Cryst.* **1990,** 46, (9), 1598-1599.
36. Winiarz, S.; Klimczuk, T.; Cava, R. J.; Czajka, R., Nanostructure characterization of $(SmS)_{1.19}TaS_2$ by means of STM/STS. *J. Cryst. Growth* **2006,** 297, (1), 7-9.
37. Sreedhara, M. B.; Hettler, S.; Kaplan-Ashiri, I.; Rechav, K.; Feldman, Y.; Enyashin, A.; Houben, L.; Arenal, R.; Tenne, R., Asymmetric misfit nanotubes: Chemical affinity outwits the entropy at high-temperature solid-state reactions. *PNAS* **2021,** 118, (35), e2109945118.
38. Dolotko, O.; Hlova, I. Z.; Pathak, A. K.; Mudryk, Y.; Pecharsky, V. K.; Singh, P.; Johnson, D. D.; Boote, B. W.; Li, J.; Smith, E. A.; Carnahan, S. L.; Rossini, A. J.; Zhou, L.; Eastman, E. M.; Balema, V. P., Unprecedented generation of 3D heterostructures by mechanochemical disassembly and re-ordering of incommensurate metal chalcogenides. *Nat Commun* **2020,** 11, (1), 3005.
39. Fang, C. M.; Wiegers, G. A.; Haas, C., Photoelectron spectra of the late rare-earth misfit layer compounds $(LnS)_{1+x}TS_2$ (Ln = Tb, Dy, Ho; T = Nb, Ta). *Physica B* **1997,** 233, (2), 134-138.
40. Cario, L.; Johrendt, D.; Lafond, A.; Felser, C.; Meerschaut, A.; Rouxel, J., Stability and charge transfer in the misfit compound $(LaS)(SrS)_{0.2}CrS_2$: Ab initio band-structure calculations. *Phys. Rev. B* **1997,** 55, (15), 9409-9414.

41. Serra, M.; Lajaunie, L.; Sreedhara, M. B.; Miroshnikov, Y.; Pinkas, I.; Calvino, J. J.; Enyashin, A. N.; Tenne, R., Quaternary $Ln_xLa_{(1-x)}S$-$TaS_2$ nanotubes (Ln=Pr, Sm, Ho, and Yb) as a vehicle for improving the yield of misfit nanotubes. *Appl. Mater. Today* **2020,** 19, 100581.
42. Lorenz, T.; Baburin, I. A.; Joswig, J.-O.; Seifert, G., Charge Transfer Variability in Misfit Layer Compounds: Comparison of SnS-$SnS_2$ and LaS-$TaS_2$. *Isr. J. Chem.* **2017,** 57, (6), 553-559.
43. Sinha, S. S.; Sreedhara, M. B.; Tenne, R., Why do nanocrystals of 2D materials form nanotubes and why is that important? *Nano Today* **2021,** 37, 101060.
44. Stolovas, D.; Ronit Popovitz-Biro, S., S. Sinha, Ora Bitton, Dan Shahar, Reshef Tenne and; Joselevich, E., Electrical Properties of LaS-$TaS_2$ Misfit Layered Compound Nanotubes. *Isr. J. Chem.* **2021,** 61, 1-14.
45. Rouxel, J.; Meerschaut, A.; Wiegers, G. A., Chalcogenide misfit layer compounds. *J. Alloys Compd.* **1995,** 229, (1), 144-157.
46. Slough, C. G.; McNairy, W. W.; Coleman, R. V.; Drake, B.; Hansma, P. K., Charge-density waves studied with the use of a scanning tunneling microscope. *Phys. Rev. B* **1986,** 34, (2), 994-1005.
47. Chamlagain, B.; Cui, Q.; Paudel, S.; Cheng, M. M.-C.; Chen, P.-Y.; Zhou, Z., Thermally oxidized 2D $TaS_2$ as a high- κ gate dielectric for $MoS_2$ field-effect transistors. *2D Materials* **2017,** 4, (3), 031002.
48. Mori, Y.; Tanemura, S., Chemical analysis of semiconducting and metallic SmS thin films by X-ray photoelectron spectroscopy. *Appl. Surf. Sci.* **2007,** 253, (8), 3856-3859.
49. Doron-Mor, I.; Hatzor, A.; Vaskevich, A.; van der Boom-Moav, T.; Shanzer, A.; Rubinstein, I.; Cohen, H., Controlled surface charging as a depth-profiling probe for mesoscopic layers. *Nature* **2000,** 406, (6794), 382-385.
50. Shabtai, K.; Rubinstein, I.; Cohen, S. R.; Cohen, H., High-Resolution Lateral Differentiation Using a Macroscopic Probe: XPS of Organic Monolayers on Composite Au–$SiO_2$ Surfaces. *J. Am. Chem. Soc.* **2000,** 122, (20), 4959-4962.
51. Cohen, H., Chemically resolved electrical measurements using x-ray photoelectron spectroscopy. *Appl. Phys. Lett.* **2004,** 85, (7), 1271-1273.
52. Filip-Granit, N.; Goldberg, E.; Samish, I.; Ashur, I.; van der Boom, M. E.; Cohen, H.; Scherz, A., Submolecular Gates Self-Assemble for Hot-Electron Transfer in Proteins. *J. Phys. Chem. B* **2017,** 121, (29), 6981-6988.
53. Lazar, S.; Botton, G. A.; Wu, M. Y.; Tichelaar, F. D.; Zandbergen, H. W., Materials science applications of HREELS in near edge structure analysis and low-energy loss spectroscopy. *Ultramicroscopy* **2003,** 96, (3), 535-546.
54. García de Abajo, F. J., Optical excitations in electron microscopy. *Rev. Mod. Phys.* **2010,** 82, (1), 209-275.
55. Stöger-Pollach, M., Optical properties and bandgaps from low loss EELS: Pitfalls and solutions. *Micron* **2008,** 39, (8), 1092-1110.
56. Deen, P. P.; Braithwaite, D.; Kernavanois, N.; Paolasini, L.; Raymond, S.; Barla, A.; Lapertot, G.; Sanchez, J. P., Structural and electronic transitions in the low-temperature, high-pressure phase of SmS. *Phys. Rev. B* **2005,** 71, (24), 245118.
57. Menushenkov, A. P.; Chernikov, R. V.; Sidorov, V. V.; Klementiev, K. V.; Alekseev, P. A.; Rybina, A. V., Relationship between the local electronic and local crystal structures of intermediate-valence $Sm_{1-x}Y_xS$. *Jetp Lett.* **2006,** 84, (3), 119-123.
58. Fieser, M. E.; Ferrier, M. G.; Su, J.; Batista, E.; Cary, S. K.; Engle, J. W.; Evans, W. J.; Lezama Pacheco, J. S.; Kozimor, S. A.; Olson, A. C.; Ryan, A. J.; Stein, B. W.; Wagner, G. L.; Woen, D. H.; Vitova, T.; Yang, P., Evaluating the electronic structure of formal LnII ions in $LnII(C_5H_4SiMe_3)_3^-$ using XANES spectroscopy and DFT calculations. *Chem. Sci.* **2017,** 8, (9), 6076-6091.

59. Kim, T. K.; Babenko, V. P.; Novgorodov, B. N.; Kochubey, D. I.; Shaikhutdinov, S. K., Destruction of the charge density wave structure in 1T-$TaS_2$ under pyridine intercalation. *Nucl. Instruments Methods Phys. Res. Sect. A Accel. Spectrometers, Detect. Assoc. Equip.* **1998,** 405, (2), 348-350.
60. Kochubey, D. I.; Kim, T. K.; Babenko, V. P.; Shaikhutdinov, S. K., Charge density waves in 1T-$TaS_2$: an EXAFS study. *Phys. B Condens. Matter* **1998,** 252, (1), 15-20.
61. Tsuchiya, T.; Imai, H.; Miyoshi, S.; Glans, P.-A.; Guo, J.; Yamaguchi, S., X-Ray absorption, photoemission spectroscopy, and Raman scattering analysis of amorphous tantalum oxide with a large extent of oxygen nonstoichiometry. *Phys. Chem. Chem. Phys.* **2011,** 13, (38), 17013-17018.
62. Cartier, C.; Hammouda, T.; Boyet, M.; Mathon, O.; Testemale, D.; Moine, B. N., Evidence for $Nb^{2+}$ and $Ta^{3+}$ in silicate melts under highly reducing conditions: A XANES study. *Am. Mineral.* **2015,** 100, (10), 2152-2158.
63. Acrivos, J. V.; Parkin, S. S. P.; Code, J.; Reynolds, J.; Hathaway, K.; Kurasaki, H.; Marseglia, E. A., Conduction band symmetry in Ta chalcogenides from Ta L edge X-ray absorption spectroscopy (XAS). *J. Phys. C: Solid State Phys.* **1981,** 14, (11), L349-L357.
64. Wachter, P., Chapter 132 Intermediate valence and heavy fermions. In *Handbook on the Physics and Chemistry of Rare Earths*, Elsevier: 1994; Vol. 19, pp 177-382.
65. Kimura, S.-i.; Mizuno, T.; Matsubayashi, K.; Imura, K.; Suzuki, H. S.; Sato, N. K., Infrared study on the electronic structure of SmS in the black phase. *Physica B:* **2008,** 403, (5), 805-807.
66. Svane, A.; Santi, G.; Szotek, Z.; Temmerman, W. M.; Strange, P.; Horne, M.; Vaitheeswaran, G.; Kanchana, V.; Petit, L.; Winter, H., Electronic structure of Sm and Eu chalcogenides. *phys. stat. sol. (b),* **2004,** 241, (14), 3185-3192.
67. Yan-Bin, Q.; Yan-Ling, L.; Guo-Hua, Z.; Zhi, Z.; Xiao-Ying, Q., Anisotropic properties of $TaS_2$. *Chinese Phys.* **2007,** 16, (12), 3809-3814.
68. Winterlik, J.; Fecher, G. H.; Felser, C.; Jourdan, M.; Grube, K.; Hardy, F.; von Löhneysen, H.; Holman, K. L.; Cava, R. J., Ni-based superconductor: Heusler compound $ZrNi_2$\Ga. *Phys. Rev. B* **2008,** 78, (18), 184506.
69. Liu, H.; Huangfu, S.; Zhang, X.; Lin, H.; Schilling, A., Superconductivity and charge density wave formation in lithium-intercalated 2H-$TaS_2$. *Phys. Rev. B* **2021,** 104, (6), 064511.
70. Reefman, D.; Baak, J.; Brom, H. B.; Wiegers, G. A., Superconductivity in misfit layer compounds $(MS)_nTS_2$. *Solid State Commun.* **1990,** 75, (1), 47-51.
71. Ashcroft, N. W., and N. David Mermin, *Solid state physics*. Saunders College Publishers: Cornell University, 1976.
72. Tidman, J. P.; Singh, O.; Curzon, A. E.; Frindt, R. F., The phase transition in 2H-$TaS_2$ at 75 K. *Philos. Mag.* **1974,** 30, (5), 1191-1194.
73. Stevens-Kalceff, M. A.; Liu, Z.; Riesen, H., Cathodoluminescence Microanalysis of Irradiated Microcrystalline and Nanocrystalline Samarium Doped BaFCl. *Microsc. Microanal.* **2012,** 18, (6), 1229-1238.
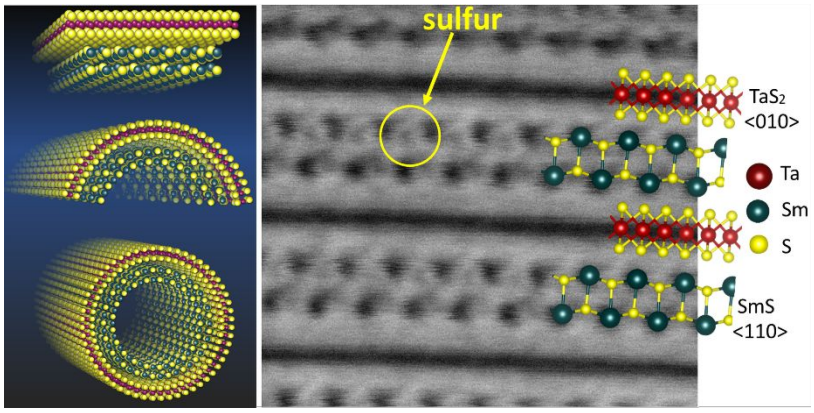
**TOC Graphic**